Birgit Kammlander, BSc

Synthesis and Characterization of Perylene-Thiophene-Perylene Non-Fullerene Acceptors and its Application in Organic Photovoltaics

MASTER'S THESIS

to achieve the university degree of

Diplom-Ingenieurin

Master's degree programme: Advanced Materials Science

submitted to

Graz University of Technology

Supervisor

Univ.-Prof. Dipl.-Ing. Dr.techn. Gregor Trimmel
Institute for Chemistry and Technology of Materials

Graz, September 2020

AFFIDAVIT

I declare that I have authored this thesis independently, that I have not used other than the declared sources/resources, and that I have explicitly indicated all material which has been quoted either literally or by content from the sources used. The text document uploaded to TUGRAZonline is identical to the present master's thesis.

Date, Signature

Contents

List of Abbreviations

AcOH	Acetic acid
BHJ	Bulk heterojunction
CB	Chlorobenzene
$CDCl_3$+TMS	Deuterated chloroform with tetramethylsilane
CH	Cyclohexane
DCM	Dichlormethane
EA	Ethylacetate
EBL	Electron blocking layer
E_g^{opt}	Optical bandgap
ETL	Electron transport layer
EQE	External quantum efficiency
FF	Fill factor
FT-IR spectroscopy	Fourier transformed infrared spectroscopy
HBL	Hole blocking layer
HOMO	Highest occupied molecular orbital
HTL	Hole transport layer
J_{SC}	Short-circuit current
KOAc	Potassium acetate
λ_{max}	Maximum absorbance wavelength
LUMO	Lowest unoccupied molecular orbital
MeOH	Methanol
MPP	Maximum power point
NFA	Non-fullerene acceptor
NMR spectroscopy	Nuclear magnetic resonance spectroscopy
PBDB-T	Poly[(2,6-(4,8-bis(5-(2-ethylhexyl)thiophen-2-yl)-benzo[1,2-b:4,5-b′]dithiophene))-alt-(5,5-(1′,3′-di-2-thienyl-5′,7′-bis(2-ethylhexyl)benzo[1′,2′-c:4′,5′-c′] dithiophene-4,8-dione)]
PCE	Power conversion efficiency
PMI	Perylenemonoimide 2-(2,6-diisopropylphenyl)-1H-benzo[10,5]anthra[2,1,9-def]iso-quinoline-1,3(2H)-dione
PMI-3HT-PMI	8,8′-(3-hexylthiophene-2,5-diyl)bis(2-(2,6-diisopropylphenyl) -1H-benzo[10,5]anthra[2,1,9-def]isoquinoline-1,3(2H)-dione)

PMI-Bpin	2-(2,6-diisopropylphenyl)-8-(4,4,5,5-tetramethyl-1,3,2-dioxaborolan-2-yl)-1H-benzo[10,5]anthra[2,1,9-def]isoquinoline-1,3(2H)-dione
PMI-Br	8-bromo-2-(2,6-diisopropylphenyl)-1H-benzo[10,5]anthra[2,1,9-def]isoquinoline -1,3(2H)-dione
PMI-DHT-PMI	8,8′-(3,4-dihexylthiophene-2,5-diyl)bis(2-(2,6-diisopropylphenyl)-1H-benzo[10,5]anthra[2,1,9-def]isoquinoline-1,3(2H)-dione)
PMI-PMI	2,2′-bis(2,6-diisopropylphenyl)-1H,1′H-[8,8′-bibenzo[10,5]anthra[2,1,9-def]isoquinoline]-1,1′,3,3′(2H,2′H)-tetraone
TGA	Thermogravimetric analysis
TLC	Thin layer chromatography
UV-vis	Ultraviolett-visual
V_{OC}	Open-circuit voltage
XRD	X-ray diffraction

Abstract

The everlasting climate change leads to a demand for developing new ways for the usage of renewable resources. For example, solar cells are making use of the sun light as energy source. While commonly used silicon wafer-based solar cells are close to their natural efficiency limit, other investigated solar cell types like organic solar cells showed great enhancement of the power conversion efficiency in the past already and are still giving a promising outlook to further improvement. Generally, in contrast to other solar cell types, organic solar cells consist of a donor and an acceptor semiconductor. Thus, there is a wide variety of possible donor and acceptor semiconductors and donor-acceptor material combinations. Furthermore, the introduction of the so-called bulk heterojunction (BHJ) systems (an inter-penetrating network of donor and acceptor material) already resulted in improvements in the past.

In this thesis, two new acceptor semiconductors were synthesized and used in organic solar cells. Both materials had an acceptor-donor-acceptor molecular structure. The two acceptor units were for both materials perylenemonoimide (PMI) and the donor unit was 3-hexylthiophene for one and 3,4-dihexylthiophene for the other material. Both materials were successfully synthesized and characterized regarding their optical and electronic properties via UV-vis spectroscopy, fluorescence spectroscopy and thermogravimetric analysis. The purity and the structure were proved via NMR spectroscopy. Furthermore, density functional theory (DFT) calculations were done to determine the optical and geometric properties of both materials.

Moreover, both materials were used together with the donor polymer PBDB-T in a bulk heterojunction system. The performance was measured using current-voltage measurements, external quantum efficiency measurements and maximum power point tracking. Additionally, UV-vis measurements were done for the thin films of both acceptor materials, as well as for the acceptor-donor mixtures. Furthermore, the crystallinity was analyzed via x-ray diffraction (XRD).

The solar cells were optimized regarding the concentration, annealing and layer thickness. The maximum power conversion efficiencies reached were 3.42% for PMI-3,4-dihexylthiophene-PMI and 0.87% for PMI-3-hexylthiophene-PMI. Annealing lead to performance improvement for both acceptor materials while light-soaking did either not have a significant effect or decreased the performance of the solar cells.

Kurzfassung

Um den voranschreitenden Klimawandel einzudämmen, ist die Nutzung erneuerbarer Energieressourcen und daher auch die Weiterentwicklung der damit verbundenen Technologien von großer Bedeutung. Eine dieser Technologien sind Solarzellen, welche sich die Sonnenenergie zunutze machen. Während die üblicherweise verwendeten siliziumbasierten Solarzellen nahe an ihrem natürlichen Effizienzlimit sind, zeigten andere Solarzellenarten wie etwa organische Solarzellen in der Vergangenheit bereits enorme Verbesserungen der Effizienzen und weisen immer noch vielversprechende Möglichkeiten zu weiterer Verbesserung auf. Im Gegensatz zu anderen Solarzellenarten bestehen organische Solarzellen aus einem Donor- und einem Akzeptor-Halbleiter. Daraus ergibt sich eine weite Bandbreite möglicher Akzeptor- und Donormaterialien sowie deren Kombinationen. Des Weiteren führte die Entwicklung der Bulk Heterojunction (BHJ), ein interpenetrierendes Netzwerk des Donor- und Akzeptormaterials, ebenfalls zu signifikanten Verbesserungen in der Vergangenheit.
In dieser Arbeit wurden zwei neue Akzeptor-Halbleiter synthetisiert und in organischen Solarzellen verbaut. Beide Materialien zeigen eine Akzeptor-Donor-Akzeptor Molekülstruktur. Die beiden Akzeptoreinheiten waren für beide Materialien Perylenmonoimid (PMI) und die Donoreinheit bestand aus 3-Hexylthiophen oder 3,4-Dihexylthiophen. Beide Materialien wurden erfolgreich hergestellt und charakterisiert bezüglich der optischen und elektronischen Eigenschaften mittels UV-vis Spektroskopie, Fluoreszenzspektroskopie und thermogravimetrische Analyse. Die Reinheit und Struktur wurde mittels NMR-Spektroskopie nachgewiesen. Des Weiteren wurden Dichtefunktionaltheorie (DFT) Berechnungen für die Bestimmung der theoretischen optischen und geometrischen Eigenschaften beider Moleküle durchgeführt. Zusätzlich wurde die Kristallinität mittels Röngtenbeugung (XRD) bestimmt.
Weiters wurden beide Materialien zusammen mit dem Donorpolymer PBDB-T als BHJ in Solarzellen verbaut und die Leistung wurde mittels Strom-Spannungsmessungen, externer Quanteneffizienzmessungen sowie Maximalpunktsmessungen bestimmt. Zusätzlich wurden noch UV-vis Messungen der Dünnschichten beider Akzeptormaterialien sowie der Akzeptor-Donor-Mischung durchgeführt.
Die Solarzellen wurden bezüglich der Konzentration, Temperung sowie der Schichtdicke optimiert. Die maximale Effizienz war 3.42% für die Solarzellen, die mit dem Akzeptormaterial PMI-3,4-Dihexylthiophen-PMI verbaut wurden, während bei PMI-3-Hexylthiophen-PMI nur eine Effizienz von 0.87% erreicht werden konnte. Das Temperieren der Solarzellen führte in beiden Fällen zu einer Verbesserung, während Light-Soaking praktisch keinen Einfluss hatte.

Acknowledgements

First of all, I would like to thank my supervisor Professor Gregor Trimmel for giving me the opportunity to write my thesis about such an interesting topic. Generally, I want to thank all my colleagues from the institute for their inputs and advice in encouraging discussions. Furthermore, I want to specifically thank Dr. Matīss Reinfelds for his help in organic synthesis and DI Bettina Schweda, DI Peter Fürk and DI Stefan Weber for their insights in organic solar cells.
Additionally, I would like to thank Ing. Josefine Hobisch, Dr. Petra Kaschnitz, Dr. Petra Hofstadler, Dr. Thomas Rath and Tobias Burger, MSc, for helping me with several measurements and discussing the results with me. I also want to thank the Austrian Klima- und Energiefonds for their financial support in the project ALTAFOS (FFG No. 865 072).
Besides the working group, I am grateful for the emotional support of my friends and my family, who always encouraged me in pursuing my goals throughout my education and helped me to re-charge during my free time.

1 Introduction

Changes in the atmospheric composition have resulted in observable global climate changes since the Industrial Revolution. One major contributor to this development is the excess use of fossil fuels and the associated emission of the green house gas CO_2. In numbers, the global average temperature has risen 0.85°C and the atmospheric CO_2 content shows a 40 % increase since 1850. [1] Global warming influences not only the average temperature, but has a wide range of different negative impacts and feedback loops. For example, higher average temperatures lead to a rise in the mean sea temperature, which impacts the ocean current and in consequence also the likelihood of emerging hurricanes. Furthermore, the increasing risk of other extreme weather conditions like droughts or heavy rains is another side-effect of climate change. This impacts the profitability of agriculture and therefore also economy. In conclusion, climate change influences economy, flora and fauna and social aspects like future living conditions.

Therefore, the development of alternative, more sustainable energy resources is a major contribution in slowing down, or in the best case scenario stopping, climate change. Additionally, the global energy demand is increasing steadily while the unsustainable energy sources nuclear energy and fossil fuels are problematic. The use of fossil fuels emits CO_2, which is a major cause of climate change. Nuclear energy, on the other hand, shows unsolved problems regarding safety and nuclear waste disposal. Nuclear energy and fossil fuels are covering 85 % of the energy demand in the European Union. [2] The other sources for energy generation are wind, water, biofuels, and solar energy. However, only 0.6% of the energy was produced by solar energy in the European Union in 2016 and only 0.3% in 2017 in Austria. [2] In other words, there is potential to higher coverage by renewable resources in general and by solar energy in specific.

More than 90 % of the global solar cell market is covered by wafer-based (mono- or poly-) crystalline silicon photovoltaics. [3] The highest efficiency reached so far for the typical p-type polycrystalline silicon solar cell was achieved by Haase et al. in 2018 with 26.1 %. [4] In 2017, Yoshikawa et al. achieved an power conversion efficiency of 26.7 % for a heterojunction solar cell construction, using amorphous and crystalline silicon. [5] The theoretical upper limit is the so-called Shockley-Queisser limit, which suggests a maximum of 29.1 %. [5] This shows, that the maximum conversion efficiency is almost reached and that the room for further improvement is limited.

Although crystalline silicon solar cells exhibit good efficiencies, there is still room for improvement. For one, those solar cells with high efficiencies need monocrystalline silicon (frequently even specific crystal orientation), which goes hand in hand with more difficult production, resulting in higher costs. [6]
In comparison, organic solar cells provide the advantages of easy fabrication and use of

very thin layers, resulting in the possibility of low weight solar cells. Nonetheless, organic solar cells have one major difficulty: low stability, leading to the necessity of encapsulating the solar cells to impede degradation through ambient air exposure. [7] Furthermore, organic solar cells show a maximum of 17.36 % efficiency. [8] Research on organic solar cells improved the performance in the past already significantly and there are still promising outlooks on further improvement.

In contrast to silicon solar cells, organic solar cells consist of two organic semiconductors: one being the electron donor material and one being the electron acceptor material. [7] Since there is a wide range of possible organic donor and acceptor materials, the band gap can be adjusted easily and there are many options for matching donor and acceptor materials. Generally, there are two main groups within the acceptor materials: fullerene and non-fullerene based acceptors. While the popular fullerene acceptors are already widely investigated, non-fullerene acceptors (NFA) are under research and provide an even wider range of possibilities.
Popular non-fullerene acceptor materials like perylenediimide (PDI) derivatives have been researched already in depth while perylenemonoimide (PMI) based acceptors are largely unexplored so far, yet promising. Therefore, PMI based acceptors have been chosen to be researched in this thesis. The investigated acceptor materials here are built as PMI-Linker-PMI units. Since promising efficiencies of 2.57 ± 0.11 have been reached in a previous master thesis with the acceptor material PMI-3-hexylthiophene-PMI, [9] this material was again synthesized and compared with 3,4-dihexylthiophene (DHT) as a linker compound due to the likeness between the linker molecules. Both linker molecules were attached on PMI units by Suzuki Coupling and subsequently tested in organic solar cells.

2 Theoretical Background

2.1 Organic Solar Cell Architecture

In general, the organic solar cell is built up by two semiconductors - the donor and the acceptor semiconductor. When exposed to light, the donor material forms an electron-hole pair, a so-called exciton, through photon absorption. [10] At the interface to the acceptor, the exciton can dissociate to mobile charge carriers and the excited electron can move from the acceptor material towards the cathode, while the hole in the HOMO level of the donor can move towards the anode. [10] The other possibility is, that the light is absorbed by the acceptor material: In this case, the exciton is formed in the acceptor material and the charge carriers move towards their respective electrodes starting at the HOMO and LUMO level of the acceptor.
This working principle lead to the development of two basic active layer concepts of organic solar cells: bilayer and bulk heterojunction, illustrated in Figure 1.
Compared to bilayer solar cells, the active layer in bulk heterojunction photovoltaics is an interpenetrating donor-acceptor network, leading to a larger interface area compared to the bilayer design. [11] Since organic semiconductors show low dielectric constants, the exciton formed exhibits a large binding energy, which results in low diffusion lengths of only approximately 10 nm. [10] Therefore, the donor-acceptor phase separation should be within 10-20 nm to impede possible recombination of the exciton. [12] Charge transfer occurs due to the potential difference between the acceptor and donor material. [12] Thus, higher interface area between the donor and the acceptor phase can increase the exciton dissociation and decrease the recombination likelihood. [12] Due to the higher interface area, bulk heterojunction organic solar cells can show improved power conversion efficiencies. [12]
However, charge recombination can also happen during the electron and hole movements to their corresponding electrodes. [12] Furthermore, the interpenetrating network has to be continuous: The donor material acts as a hole pathway and the acceptor material as an electron pathway to the corresponding electrodes. [12] Thus, if the network in the active layer is not built up sufficiently, the charge carriers cannot reach their electrodes. Therefore, the morphology of the bulk heterojunction plays an important role to achieve high power conversion efficiencies.

However, investigations to increase the diffusion length have been made and can lead to better efficiencies in the bilayer construction. For example, larger crystalline domains (100 nm vs 400 nm) of the active layer materials increased the 1D diffusion length by 18.5 nm (6.5 nm vs 25 nm) for PTCDA (3,4,9,10-perylenetetracarboxylic dianhydride). [13] Lee et al. also reported good exciton diffusion in bilayer constructed solar cells due to long-range energy transfer between the two active layers: A great density of charge-transfer states was verified by electroluminescene measurements. [14] Furthermore, of-

ten used thermal annealing increases the crystallinity of the films as well: While the P3HT (poly(3-hexylthiophene-2,5-diyl)) film without thermal treatment showed a diffusion length of 3.3 nm, the thermal treatment at 235 °C lead to an increase of 3.7 nm. [15] Additionally, Yang et al. were able to show that optimized, annealed bilayer solar cells performed better than their annealed BHJ counterparts regarding their bimolecular recombination losses: The charge carrier lifetimes were compared at different voltages, which showed that the lifetime was lower for the BHJ solar cells and significantly higher for bilayer devices. [16] Thus, recombination losses were lower for the bilayer construction, likely due to the non-existing "dead ends" which might occur in BHJ devices. [16]

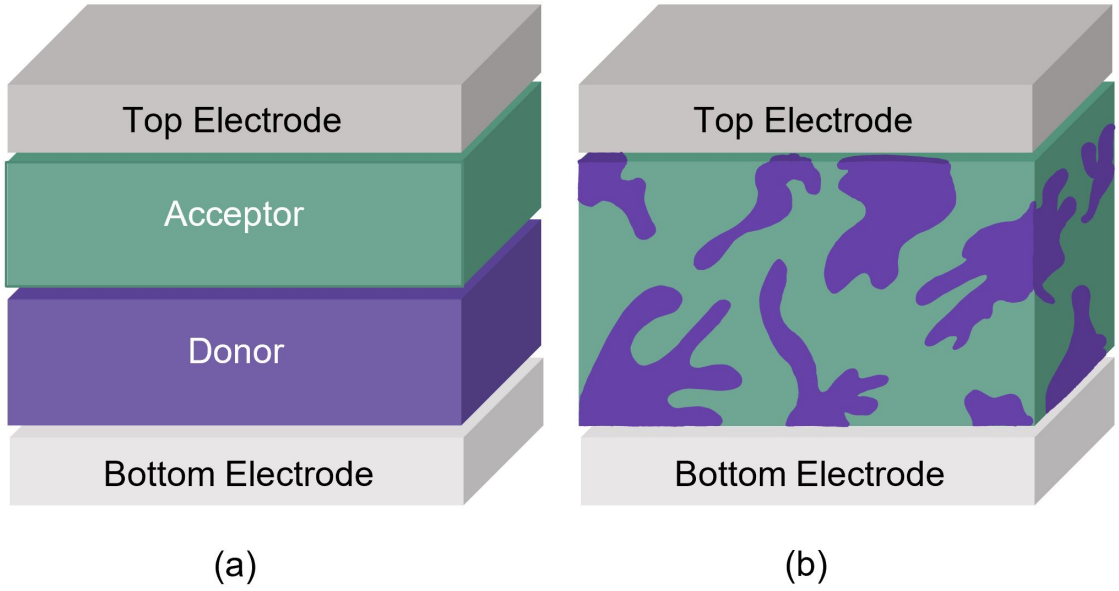

Figure 1: Schematic illustration of (a) a bilayer organic solar cell and (b) a bulk heterojunction organic solar cell

Furthermore, both active layer concepts (bilayer and BHJ) are constructed either using the normal or the inverted design. [11] If the top electrode of Figure 2 (a) is the cathode (electron selective electrode, i.e. aluminium) and the bottom electrode is the anode (hole selective electrode, i.e. indium tin oxide/ poly(3,4-ethylenedioxythiophene)-poly(styrenesulfonate (ITO/PEDOT:PSS)), it is called a normal device architecture. [11] If, on the other hand, the top electrode is the anode (i.e. MoO_x/silver) and the bottom electrode is the cathode (i.e. ZnO/ITO), it is called inverted design. [11] Hence, the difference between both architectures is the charge carrier movement direction. If the normal device design is carried out with common metal cathodes (i.e. Al, Ca), more expensive encapsulation than for the inverted design is needed, due to the more likely oxidation of the cathode metal under ambient air conditions. [11] In the inverted design, the top electrode materials commonly used are high work function metals like silver or gold due to their non-degrading properties under oxygen influence. [17] However, encapsulation is needed for the common inverted design as well: Corazza et al. showed for P3HT:PCBM (P3HT:[6,6]-phenyl C_{61} butyric acid methyl ester) active layers, that, in comparison to the

normal device structure, the unencapsulated inverted design organic solar cells had enhanced stability regarding humidity but lower stability if tested under light-soaking. [18] The encapsulated inverted devices on the other hand performed better under light exposure than the normal devices. [18]
Furthermore, in the normal device architecture, the commonly used PEDOT:PSS promotes the diffusion of indium of the ITO layer into the donor-acceptor layer and can result in interface instability. [19] The inverted design on the other hand allows the avoidance of PEDOT:PSS and therefore this issue is solved for inverted devices. [11]

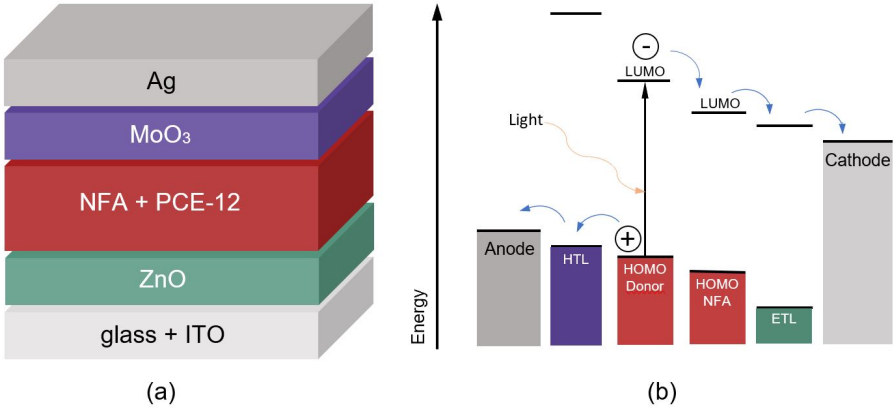

Figure 2: Illustration of (a) the device architecture and (b) the solar cell work mechanism and energy levels of the different layers

In Figure 2 (a), one can see the device architecture of the constructed solar cells for this thesis, using the inverted design. The bottom layer, being glass + ITO (indium tin oxide), operates as the cathode. Besides easy electron transportation, transparency is an advantageous characteristic for anodes in the inverted design. [20] Due to its transparency and conductivity, ITO is widely used in OSCs. [11] Compared to other transparent conductive oxides, like gallium doped zinc oxide or zinc doped indium-oxide, sheet resistivity and hole mobility of ITO is less influenced by thermal treatment. [21]

Generally, interlayers are necessary in organic solar cells to improve charge carrier collection [22], thus enhancing the solar cell performance. [23] Hence, the following layer is zinc oxide (ZnO), which acts as an electron transport layer (ETL) and hole blocking layer (HBL). ZnO exhibits a wide band gap of 3.3 eV and is a n-type material. [17] In more detail, ZnO inhibits intrinsic defects, i.e. oxygen vacancies or additional zinc on interstitial sites. [17] Additionally, the conductivity depends on the crystallinity, which depends further on the annealing temperature used. [24] Furthermore, the conductivity of the interlayer is not only determined by the annealing temperature, but also by the atmosphere (i.e. oxygen exposure). [17]

The subsequent layer is the donor-acceptor bulk. Further details will be described in section 2.3 and section 2.2.

The following molybdenum oxide (MoO_X) layer serves as a hole tranport layer (HTL) and electron blocking layer (EBL). Additionally, diffusion processes of the anode material and oxygen into the active layer can be intervened by this layer. [25]

Lastly, the silver anode follows. Compared to other metallic cathode materials like Ca or Mg, Ag is not easily oxidized. [11] Due to this, Ag is a commonly used anode material in inverted bulk heterojunction solar cells.

2.2 Donor material

The use of polymers gives a wide range of possible donor materials [26], as can be seen in Figure 3, which depicts several common donor materials. [27] The first polymer donors, like MEH-PPV (poly[2-methoxy-5-(2-ethylhexyloxy)-1,4-phenylenevinylene]), P3HT (Poly-3-hexylthiophene) or POPT (poly(3-(4-n-octyl)-phenylthiophene)) are widegap materials and show low short circuit current and thus only limited efficiency. [26] While MEH-PPV showed additionally low charge mobility, leading to low efficiencies with PCBM of 2.9 %, [28] P3HT overcame this problem due to its characteristics regarding solubility, self-assembly, charge carrier mobility and crystallinity. [29] However, the power conversion efficiency was still limited to 7.5 %, [30] due to the large bandgap. [26]

Due to the natural limitation given by the wide band gap, medium band gap donor materials were investigated. For example, PTB7 (tPoly [[4,8-bis[(2-ethylhexyl)oxy] benzo[1,2-b:4,5-b']dithiophene-2,6-diyl][3-fluoro-2-[(2-ethylhexyl)carbonyl]thieno[3,4-b] thiophenediyl]]) has a band gap of 1.6 eV and has a good hole mobility due to its quinoidal structure and the side chains enable good solubility. [26]

The third possibility, small band gap donor materials, show again high hole mobility and in the case of BDT (benzo[1,2-b:4,5-b']dithiophene) based donors also the advantage of small steric hindrance. [26] This results in a minimum influence of neighbouring units on the energy levels of the band gap of the donor. [26]

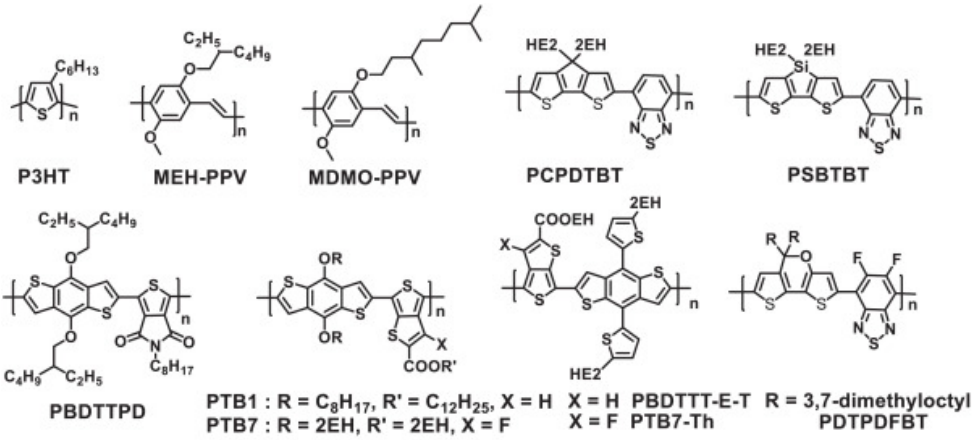

Figure 3: Illustration of several common donor materials [27]

PBDB-T based donor materials exhibit low HOMO levels, which can result in greater open circuit voltages: The open circuit voltage is determined by the difference between the donor HOMO and the acceptor LUMO level. [31] Therefore, if the acceptor material exhibits a high LUMO level compared to the HOMO level of PBDB-T, enhanced open-circuit voltages can be observed. Furthermore, implementing fluorine atoms in the side groups can increase the PCE by shifting the HOMO level of the PBDB-T donor. [31] Chlorination or substituition of the thiophene blocks can also lead to increased PCEs. [31] PBDB-T derivatives show great charge generation, high fill factors and good morphology characteristics. [31] Due to these reasons and the HOMO-LUMO level match between PBDB-T and the acceptor materials synthesized, PBDB-T was used in this thesis as the donor material.

2.3 Acceptor material

In general, two classes of acceptor materials can be differentiated in organic solar cells: Fullerene and non-fullerene acceptors. [32] Fullerene acceptors have been investigated in more depth sooner than their non-fullerene counterparts.
Two popular fullerene acceptors are depicted in Figure 4. These show on one hand high electron mobilities, while on the other hand the band gap is large and the absorption spectra is rather narrow compared to non-fullerene acceptors, meaning light absorbance is low. [26] Otherwise, fullerenes and their derivatives also have high electron affinity, the electron diffusion length is comparatively long and the exciton dissociation happens quickly. [26] Furthermore, due to their fully-conjugated, spherical structure, they show the advantage of isotropic electron transport, which enhances electron de-localization at the donor-acceptor surfaces. [33]

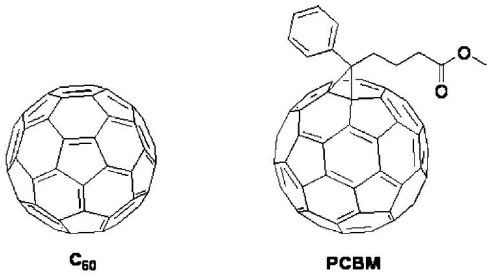

Figure 4: Illustration of two fullerene acceptors: C_{60} and PCBM, Reprinted by permission from Springer Nature: Springer Nature, Photosynthesis Research (Organic Solar Cells: An Overview Focusing on Active Layer Morphology, Travis L. Benanti et al, (Jan 9, 2006)

Non-fullerene acceptors in comparison have the major advantage of tunable energy levels and broad absorption range in the visible region, but do have low electron mobilities. [26] Furthermore, it appears that morphology control is a major necessity to achieve high and reproducible power conversion efficiencies. [34] On the other hand, while using low driving energies on fullerene based acceptors leads to high photocurrents but low photovoltages, non-fullerene based acceptors depict only little voltage losses while maintaining high photocurrents. [34]
One major difficulty in comparison to their fullerene counterparts is the anisotropic structure. [34] The necessary charge transfer and transport is relying on the $\pi - \pi$ interactions between donor and acceptors and thus on the molecular orientation. [34]

Generally, non-fullerene acceptors can be classified by their chemical structure in aromatic diimides and structures using the electron push-pull effects. [34] In Figure 5, the two different classes of non-fullerene acceptors are depicted in **a** and **b**. Next to the two structures in **a**, the composition can be seen: For the acceptor to work properly, the conjugated backbone has to be connected with an electron pushing organic group. [34] This atom is then linked (via a conjugated structure) to a highly electron pulling organic group. [34]

Light exposure on this structure leads to charge transfer from the conjugated linkage to the conjugated backbone.
As can be seen further in Figure 5 **c**, **d**, **e** and **f**, PCEs for small molecule acceptors were already 9.5 %, for polymeric diimides 9.18 % and for ITIC derivatives 13.1 %.

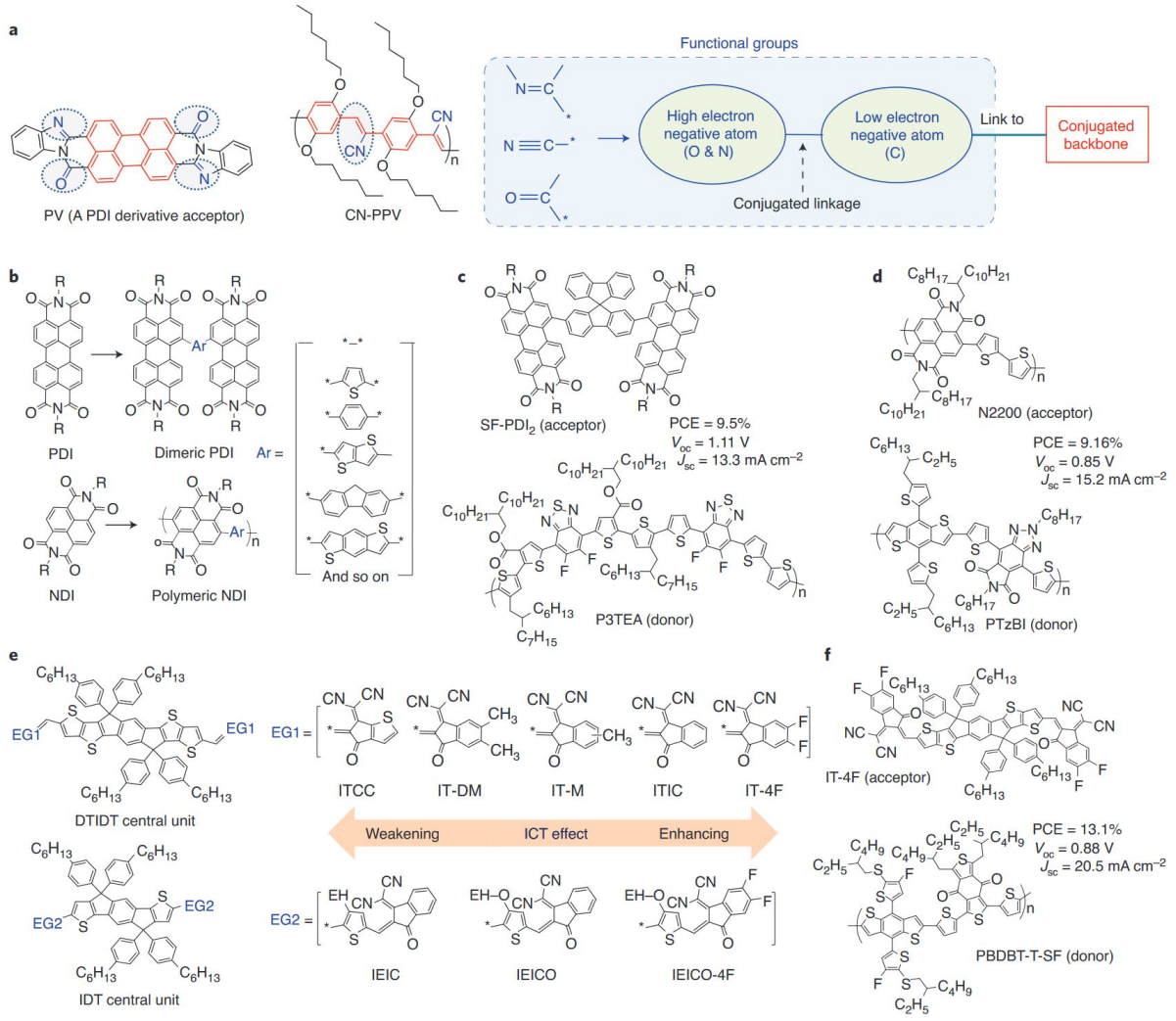

Figure 5: Well-known non-fullerene acceptors; (a) PV and CN-PPV: linkage to low and high electron negative atoms; (b) typical PDI derivatives linked via Aryl; (c) Small molecule diimides with corresponding donor and their photovoltaic characteristics; (d) Polymeric diimides with used donor and their photovoltaic characteristics; (e) ITIC derivatives (f) ITIC derivatives and the photovoltaic characteristics, Reprinted by permission from Springer Nature: Springer Nature, Nature Materials, (Organic solar cells based on non-fullerene acceptors, Jianhui Hou et al), (2018), 08 August 2020 (doi: 10.1038/NMAT5063.)

Additionally, in Figure 5 **b** PDI-based acceptors are illustrated: Perylene-based acceptors are advantageous regarding their stability under ambient conditions and their modularity. [35] Furthermore, the lifetime of the excited singlet state is long, leading to higher chance for charge dissociation. [35]

In contrast to fullerene and the non-fullerene perylenediimide (PDI) acceptors, perylenemonoimide (PMI) acceptors are not investigated thoroughly yet despite their high absorptivities and fluorescence, [36] their high stability and low LUMO. [37] Furthermore, comparing PMI and PDI, both exhibit strong absorption and in both derivatives, the influence of the necessary substituents to enhance solubility on the absorption and emission are neglect-able due to the node formation at the imide positions in the HOMO and LUMO state. [35]
Compared to PDI, PMI acceptors also exhibit a higher LUMO state, which can result in better open-circuit voltages if the donor material exhibits a matching HOMO level. [38]
However, large scale synthesis is more difficult for PMI derivatives than for other non-fullerene acceptors. [38] Additionally, they show $\pi - \pi$ stacking, [39] resulting in low solubility. [37]
However, PMI-Aryl-PMI acceptor molecules have been investigated by Hu et al. in 2017, as Figure 6 depicts: The highest PCE value (1.3%) was accomplished with the molecule structure **9**, thus a molecule chain of two thiophene units. [37] The structures **7**, **8**, **10**, **12**, **12** and **14** showed a PCE of 0.1 %. [37] Lastly, structure **11** achieved a PCE of 0.2 %. [37]

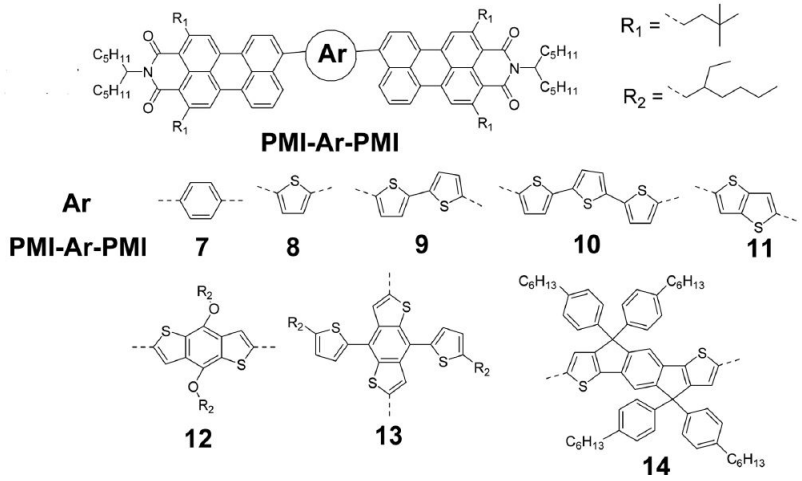

Figure 6: Illustration of PMI-Aryl-PMI acceptor materials; Reprinted with permission from (Hu, Y.; Chen, S.; Zhang, L.; Zhang, Y.; Yuan, Z.; Zhao, X.; Chen, Y. J. Org. Chem. 2017, 82 (11), 5926 5931). Copyright (2020) American Chemical Society.

In Figure 7, further investigated PMI-Linker-PMI structures can be seen:
Alibegic successfully synthesized the acceptor molecule PMI-3HT-PMI, which reached a PCE of 2.57 $\pm$0.11 in 2020 using PBDB-T as donor material with a donor-to-acceptor ratio of 1:1. [9]

Schweda investigated the PMI based acceptors using oPh, mPh, pPh and $Ph(PMI)_3$. The acceptor material PMI-oPh-PMI reached a power conversion efficiency of 0.98 %, using PBDB-T as donor material in a 1:1 ratio. [40] Although difficulties were observed regarding the solubility, PMI-mPh-PMI achieved a power conversion efficiency of 1.90$\pm$0.08. [40] PMI-pPh-PMI was even less soluble but still reached better efficiencies that PMI-oPh-PMI

with a power conversion efficiency of 1.49±0.03 with a donor-to-acceptor ratio of 1:1, using PBDB-T as donor material. [40] Lastly, a power conversion efficiency of 0.12±0.02 was achieved using PMI-Ph(PMI)$_3$ using a 1:1 donor-to-acceptor ratio with PBDB-T as donor material. [40]

In 2020, Fürk investigated the two acceptor materials PMI-F(DEG)-PMI and PMI-C(DEG)-PMI and reached 1.21±0.06 and 3.58±0.14, respectively. [41] In both cases, PBDB-T was used as donor material in a donor-to-acceptor ratio of 1:1. However, while annealing the active layer lead to a decrease in efficiency of PMI-F(DEG)-PMI, it lead to an increase for the solar cells using PMI-C(DEG)-PMI. [41] The PMI-F(DEG)-PMI solar cells on the other hand showed improved performance after light-soaking for 4 minutes. [41]

Weber et al. researched the acceptor materials PMI-F-PMI, PMI-FN-PMI and PMI-FSi-PMI in 2020: All cells were built with a donor-to-acceptor ratio of 1:0.67, using PBDB-T as donor material. [42] Furthermore, annealing lead to an increase of crystallinity, which enhanced the PCE for all three acceptors. [42] PMI-F-PMI needed the lowest annealing temperature (135 °C) to reach 4.34±0.37, PMI-FN-PMI and PMI-FSi-PMI were annealed at 150 °C and achieved 4.67±0.28 and 4.45±0.36, respectively. [42] PMI-F-PMI as acceptor material reached an even higher PCE in 2017, as reported by Zhang et al.: The organic solar cells used the donor:acceptor mixture PTZ1:PMI-F-PMI in a 2:1 ratio including the solvent additives N-methyl pyrrolidone (0.5%) and diphenyl ether (0.5%) and achieved a PCE of 6%. [43]

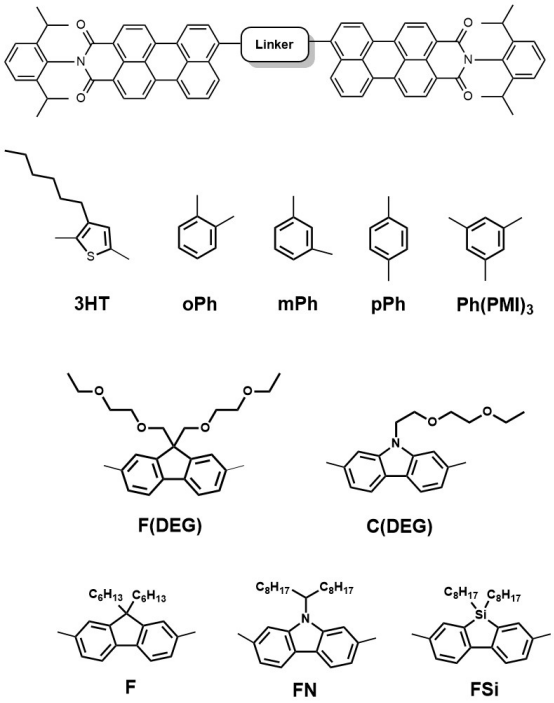

Figure 7: Illustration of PMI-Linker-PMI acceptor materials investigated by [9], [40], [41], [42]

However, the currently best organic solar cells using non-fullerene acceptors were developed by Meng et al. and Liu et al. using a tandem architecture and single cell architecture, respectively. Figure 8 depicts the device architecture as well as the used donor and acceptor materials of the tandem cell developed by Meng et al., which achieved a great PCE of 17.36%. [8] Liu et al. on the other hand blended the copolymer D18 and Y6, depicted in Figure 9, and achieved a power conversion efficiency of 17.6 %. [44]

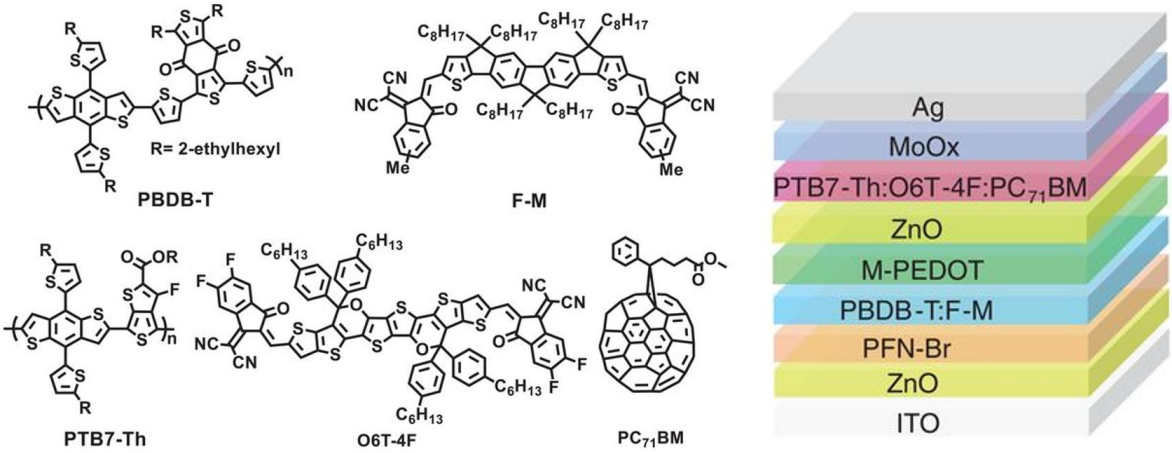

Figure 8: Chemical structures of the donor and acceptor materials of the tandem cell by Meng et al., which achieved a PCE of 17.36%, From Lingxian Meng,Yamin Zhang,Xiangjian Wan,Chenxi Li,Xin Zhang,Yanbo Wang,Xin Ke,Zuo Xiao,Liming Ding,Ruoxi Xia,Hin-Lap Yip,Yong Cao,Yongsheng Chen, Organic and solution-processed tandem solar cells with 17.3% efficiency, *Science*, vol 361, no. 6407, [8]. Reprinted with permission from AAAS.

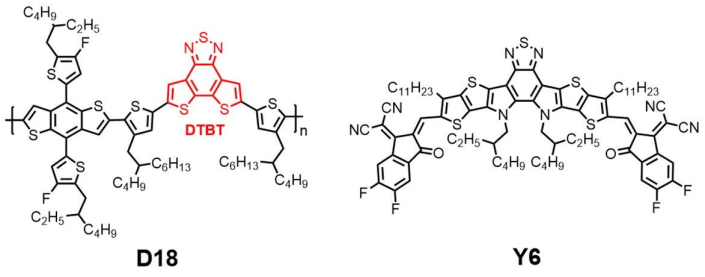

Figure 9: Chemical structures of the donor and acceptor materials of the tandem cell by Meng et al., which achieved a PCE of 17.36%, Reprinted from Science Bulletin, Vol 65, Liu Q., Jiang Y., Jin K., Qin J., Xu J., Li W., Xiong J., Liu J., Xiao Z., Sun K., Yang S, Zhang X., Ding L., 18% Efficiency organic solar cells, 272-275, Copyright (2020), with permission from Elsevier.

3 Objective

The aim of this work is to investigate two PMI based acceptor materials for organic solar cells. Due to the promising results of 2.57±0.11 of PMI-3-hexylthiophene-PMI (3HT) (see Figure 10, molecule 2) and the large Stokes-shift between absorption and emisson of 88 nm [9], this acceptor material was compared to PMI-3,4-dihexylthiophene-PMI (DHT) (see Figure 10, molecule 3) to investigate the influence of a second hexyl-chain on the optical and electrical properties. Additionally, DFT calculations were carried out for both acceptor materials to determine the optical band gap, the HOMO and LUMO energy levels and the dihedral angles. Furthermore, the behaviour in solar cells was researched for both materials. The main interest lies within possible improvements of the power conversion efficiency (PCE) by using different active layer thicknesses, annealing conditions and donor-to-acceptor ratios in the active layer.
Both acceptor materials were synthesized and characterized. In order to verify the structure and ensure sufficient quality, the synthesized materials were controlled via NMR spectroscopy. The materials were characterized regarding their optical properties (i.e. absorption coefficient, band gap) using UV-vis spectroscopy and fluorescence spectroscopy. The thermal properties were investigated using thermogravimetric analysis.
After assembling the solar cells, J-V plots were measured to gather information about the power conversion efficiency and other solar cell characteristics like the open circuit voltage. Additionally, the external quantum efficiency as well as maximum power point tracking measurements were done.

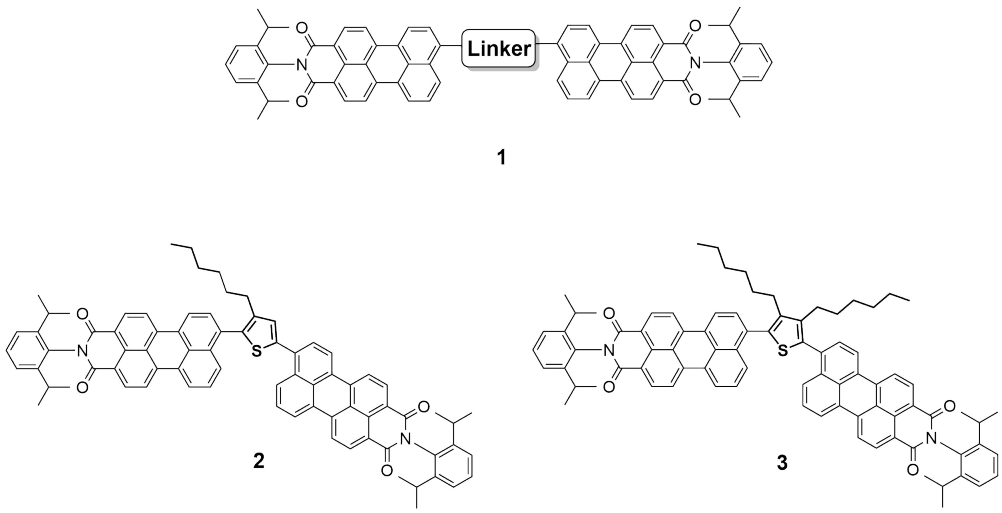

Figure 10: Chemical structures of the synthesized materials; **1** - PMI-Linker-PMI (acceptor-donor-acceptor), **2** - PMI-3HT-PMI, **3** - PMI-DHT-PMI

4 Experimental

4.1 Density Functional Theory Calculations

The softwares used can be found in Table 1.

Table 1: Softwares used for the DFT calculations

Software	Usage reason
ChemDraw 18.2	Structure Drawing
Chem3D 18.2	Pre-optimization
Gaussian 09 [45]	Geometrical Optimization, Band Gap Calculations
Avogadro	Visualization HOMO-LUMO
Notepad ++	Input File Adaption

The optical optimization was done for the flipped and non-flipped-acceptor molecules using Gaussian 09, with the 6-31+G(d,p) the functional set B3LYp. In order to reduce the computing time, the imide groups and the hexyl-chains were substituted with methyl groups. The molecule PMI-3HT-PMI was also computed one time with the hexyl-chain to ensure, that the substitution of the hexyl-chain does not result in significantly different results. Since no full conversion was reached, an UltraFine Grid was used. Generally, the procedure for the calculations was as follows:
Firstly, the structure was drawn in ChemDraw and then pre-optimized in ChemDraw3D. Subsequently. the geometrical optimization was done using Gaussian 09. Afterwards the UV-Vis absorption as well as the HOMO and LUMO levels were calculated. Lastly, the orbitals were visualized. Furthermore, the dihedral angles of the molecules were determined. The calculations were carried out together with Matīss Reinfelds.

Calculation - geometrical optimization:
#p B3LYP/6-31G(d,p) OPT=ReadFC Freq

Calulation - UV-vis spectra:
#p B3LYP/6-31+G(d,p) geom=checkpoint td(nstates=10)

4.2 Synthesis

4.2.1 General Experimental Procedure

In Table 2 the used chemicals, their suppliers and their purity grade are shown. The chemicals were all purchased from the named resources and used as received without further purification.

Synthesis Perylenemonoimidebromine (PMI-Br)

Table 2: Chemicals used for the synthesis of the acceptor materials

Chemical	Supplier	Purity grade
[1,1'Bis(diphenylphosphino)ferrocene] dichlorpalladium(II), $Pd(dppf)Cl_2$	Fluorochem	-
1,4-dioxane	Sigma Aldrich	99.8%
2,5-dibromo-3,4-dihexylthiophene	Sigma Aldrich	97%
2,5-dibromo-3-hexylthiophene	Fluorochem	-
Acetic acid, AcOH	Sigma Aldrich	99.8%
Aliquat 336	Sigma Aldrich	-
Bis(pinacolato)dibboron, Bpin-Bpin	Fluorochem	-
Bromine, Br_2	Sigma Aldrich	$\geq$ 99%
Chloroform, $CHCl_3$	Fischer Chemical	$\geq$ 99.8%
Cyclohexane, CH	VWR chemicals	100%
Deuterated chloroform with Tetramethylsilane, $CDCl_3$+TMS	Eurisotop	99.8%
Dichlormethane, DCM	Fischer Chemicals	99.8%
Ethyl acetate, EA	Fischer Chemicals	$\geq$ 99.8%
Iodine, I_2	Sigma Aldrich	$\geq$ 99.99%
Methanol, MeOH	VWR Chemicals	100%
Palladium-tetrakis(triphenylphosphine), $Pd(PPh_3)_4$	Fluorochem	-
Perylenemonoimid	TCl	98%
Potassium acetate, KOAc	Acro Organics	$>$ 99%
Sodium sulfate, Na_2SO_4	Carl Roth	$\geq$ 99%
Toluene	VWR chemicals	99.5%

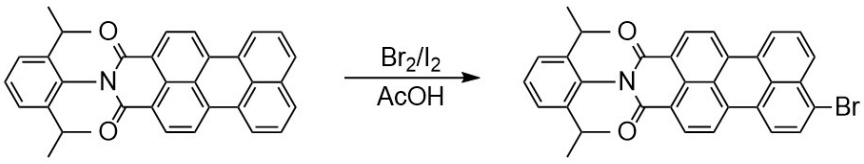

Figure 11: Synthesis route for PMI-Br

Table 3: Masses used for the Synthesis of PMI-Br

Name	**Mass / mg**	**Volume / ml**	**Amount of Substance / mmol**	**Equivalent**
PMI	4650	-	9.7	1
AcOH	-	200	-	-
I_2	103	-	0.4	0.04
Br_2	-	2	39.0	4

Both acceptor materials were synthesized using **perylenemonoimide bromide (PMI-Br)** as an educt. Therefore **PMI** was first brominated, following the reaction scheme shown in Figure 11 and using the masses declared in Table 3:
Firstly, 4650 mg **perylenemonoimide (PMI)** (9.7 mmol, 1 eqv.) was mixed with 200 ml **acetic acid (AcOH)** in a flask and stirred for 30 minutes. Subsequently, 90 mg **iodine (I_2)** (0.4 mmol, 0.04 eqv.) and 2 ml **bromine (Br_2)** (39 mmol, 4 eqv.) were added and the solution was stirred until full conversion was reached (two nights, control via TLC). Then

the product was diluted in distilled water until a pH of 5 was reached and the precipitate was filtered. The filter cake was dried in vacuum.

Yield: 3788 mg (7.87 mmol, 81%), dark red powder, $C_{34}BrNO_2$ (560.49 g/mol)

Synthesis Perylenemonoimide-borpinacolester (PMI-Bpin)

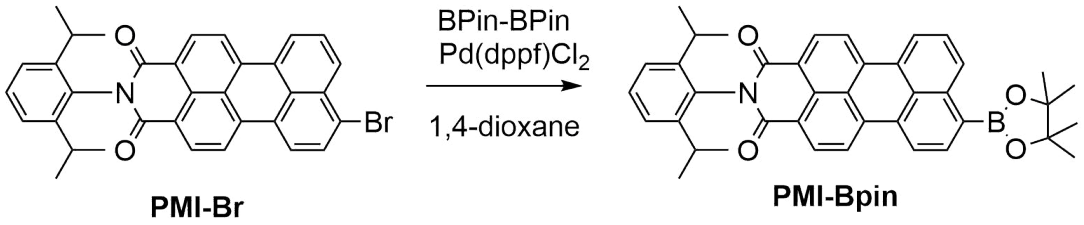

Figure 12: Synthesis route for PMI-Bpin

Table 4: Masses used for the Synthesis of PMI-Bpin

Name	Mass / mg	Volume / ml	Amount of Substance / mmol	Equivalent
PMI-Br	3788	-	6.8	1
KOAc	1991	-	20.3	3
$Pd(dppf)Cl_2$	497	-	0.7	0.09
Bpin-Bpin	2061	-	8.1	1.2
1,4-Dioxane	-	80	-	-

The transition from **PMI-Br** to **perylenemonoimide boronic acid pinacole ester (PMI-Bpin)** was done following the reaction scheme depicted in Figure 12 and using the masses declared in Table 4 as follows:
1991 mg **potassium acetate (KOAc)** (20.3 mmol, 3 eqv.) and 497 mg **tetrakis(triphenylphosphine)-palladium ($Pd(dppf)Cl_2$)** (0.7 mmol, 0.09 eqv.) were weighed in in a flask under inert conditions to prevent inactivation of the catalyst caused by oxygen exposure. [46] Then 3788 mg **PMI-Br** (6.8 mmol, 1 eqv.) and 2061 mg **bis(pinacolato)diboron (Bpin-Bpin)** (8.1 mmol, 1.2 eqv.) were added and the mixture was flushed with **nitrogen** for 30 minutes. 80 ml dry **1,4-dioxane** were added and the solution was stirred under nitrogen-flow at 80 to 90 °C over night and turned dark red.
After ensuring full conversion using TLC, the solution was first concentrated by rotary-evaporation and then extracted (3 times **dichlormethane (DCM)** and **water (H_2O)**. Then it was 3 times washed with **Brine**). The solution was dried over 2 spoons of **sodium sulfate (Na_2SO_4)** for 15 minutes and subsequently filtrated, washed with **DCM** and dried using the rotary evaporator. A recrystallization was done using 40 ml **toluene**, left over night and filtrated the next day. Two more recrystallizations were done equally.

Yield: 2155 mg, (3.55 mmol, 52%), orange powder, $C_{40}H_{38}BNO_4$ (607.56 g/mol)

4.2.2 Synthesis of PMI-3HT-PMI

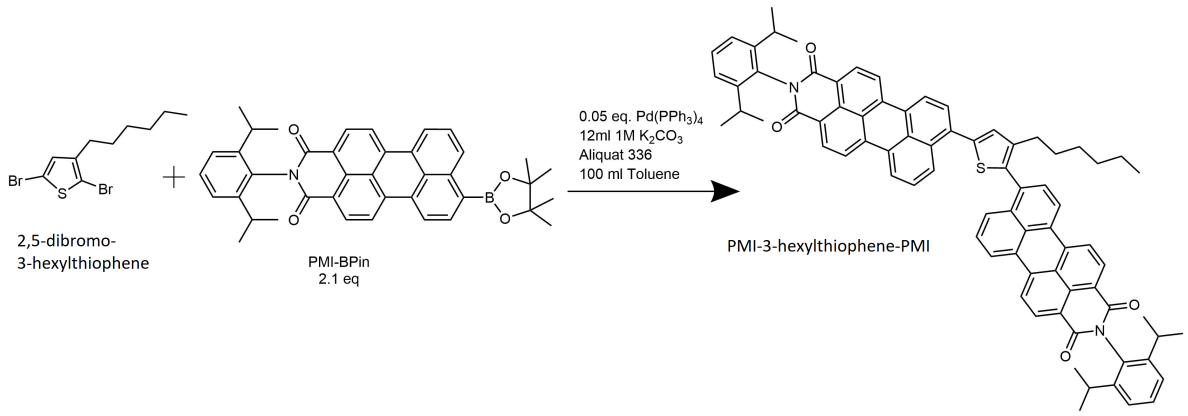

Figure 13: Reaction scheme, PMI-3HT-PMI

Table 5: Masses used for the Synthesis of PMI-3HT-PMI

Name	Mass / mg	Volume / ml	Amount of Substance / mmol	Eqv.
Dibromo-3HT	200	-	0.6	1
PMI-Bpin	893	-	1.5	2.4
$Pd(PPh_3)_4$	35.4	-	0.03	0.05
K_2CO_3	-	12	-	-
Aliquat 336	-	2-3 drops	-	-
Toluene	-	100	-	-

Figure 13 depicts the reaction scheme and Table 5 gives the amounts used in this reaction.

Firstly, 200 mg **2,5-dibromo-3-hexylthiophene (dibromo-3HT)** (0.6 mmol, 1 eqv.), 12 ml 1M **potassium carbonate (K_2CO_3)** and 2-3 drops **Aliquat 336**, to enhance reaction time [47], were put into in a flask. 893 mg **PMI-Bpin** (1.5 mmol, 2.4 eqv.) and 100 ml **toluene** were put together and stirred for 15 minutes. 12 ml (0.25 eqv.) of this mixture were transferred to the flask with the other compounds. The rest was put in a dropping funnel. Both solutions were flushed with **nitrogen** for 2 h. 35.4 mg of the catalyst, **palladium-tetrakis(triphenylphosphine) ($Pd(PPh_3)_4$)** (0.03 mmol, 0.05 eqv.), were added to the reaction flask and the solution was flushed again with **nitrogen** for 30 minutes. Subsequently, the solution was heated to 80-90°C while using a cooling funnel and after 25 minutes a TLC showed full conversion of **PMI-Bpin**. Thus, another 0.25 eq. were dropped into the reaction flask from the dropping funnel. This procedure was repeated until the needed 2.4 eqv. of **PMI-Bpin** were added.

The reaction was left over night and since the flask was free from black spots, meaning the catalyst did not oxidize over night, another 100 mg **PMI-Bpin** (0.16 mmol, 0.26 eqv.) were added to the cold solution under inert conditions. Then the mixture was again heated up to 80 - 90°C. After full conversion, the reaction mixture was cooled down and

extracted as described in section 4.2.1.

The solution was purified using **ethylacetate (EA)** or **dichlormethane (DCM)** and **methanol (MeOH)** for recrystallization, with subsequent cooling in the fridge over night. The next day **cyclohexane (CH)** was used to build two phases and improve the recrystallization process. This was done three times. Then the solution was further purified using column chromatography (with increasing concentration content of **EA** from 10% to 25%). This was verified, as can be seen in the NMR spectra in section 6 and compared with [48].

Yield: 47 mg (0.14 mmol, 23.5%), dark violet powder, $C_{78}H_{66}N_2O_4S$ (1127.45 g/mol)

^{1}H-NMR (500MHz, $CDCl_3$) δ = 8.71 - 8.67 (m, 4H), 8.60 - 8.59 (d, 1H, $^3J_{HH}$= 8.84 Hz),8.56 - 8.47 (m, 8H), 8.10 - 8.08 (d, 1H, $^3J_{HH}$= 8.24 Hz), 7.86 - 7.85 (d, 1H, $^3J_{HH}$= 8.03 Hz), 7.80 - 7.79 (d, 1H, $^3J_{HH}$= 7.81 Hz),7.77 - 7.69 (m, 2H) , 7.51 - 7.48 (t, 2H, $^3J_{HH}$= 7.74 Hz), 7.38 - 7.35 (t, 5H, $^3J_{HH}$= 7.84 Hz), 2.82 - 2.77 (sept, 4H, $^3J_{HH}$= 6.65 Hz), 2.58 - 2.55 (t, 2H, $^3J_{HH}$= 7.20 Hz), 1.67 - 1.61 (m, 3H), 1.21 - 1.20 (d, 30H, $^3J_{HH}$= 6.88 Hz), 0.81 - 0.78 (t, 3H, $^3J_{HH}$= 7.24 Hz)

FT-IR $\bar{\nu}$ (cm^{-1}): 2958, 2926, **1699, 1659 (OCNCO imide)**, 1579, 1459, 1353, 1242, 1187, 804, 751

4.2.3 Synthesis of PMI-DHT-PMI

Synthesis Approach 1

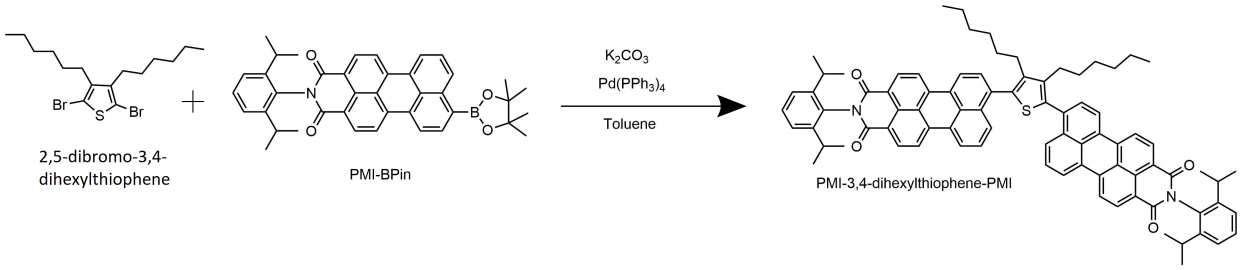

Figure 14: Reaction scheme for the synthesis of PMI-DHT-PMI, synthesis approach 1

Table 6: Masses used for the Synthesis of PMI-DHT-PMI, synthesis appraoch 1

Name	Mass / mg	Volume / ml	Amount of Substance / mmol	Eqv.
Dibromo-DHT-PMI	160	-	0.4	1
PMI-Bpin	498	-	0.8	2.1
$Pd(PPh_3)_4$	23	-	0.02	0.05
K_2CO_3, 1M	-	1.8	-	-
Aliquat 336	-	2-3 drops	-	-
Toluene	-	18	-	-

The first approach, see Figure 14 and Table 6, was to weigh in **2,5-dibromo-3,4-dihexylthiophene (dibromo-DHT)** (160 mg, 0.4 mmol, 1 eqv.), **potassium carbonate (K_2CO_3)** (1.8 ml), **Aliquat 336**, **toluene** (18 ml) and 2.1 eqv. of **PMI-Bpin** (498 mg, 0.8 mmol) in a flask. Then the mixture was twice flushed with **nitrogen**. Subsequently the catalyst, **palladium-tetrakis(triphenylphosphine) ($Pd(PPh_3)_4$)** (23 mg, 0.02 mmol, 0.05 eqv.), was added under inert conditions. Afterwards the mixture was heated to 80-90°C under inert conditions and full conversion was reached the next day. After extraction, another TLC was done and showed many by-products. During purification it turned out, that the reaction did not result in sufficient amount of the desired product. This suggested, that adding **PMI-Bpin** in excess favours conversion to the side-product **perylenemonoimide-perylenemonoimide (PMI-PMI)** more than the reaction to the desired product. Thus, another approach was tried.

Synthesis Approach 2

Figure 15 illustrates the reaction route, that was tried as a next approach. The masses can be found in Table 7. Firstly, **2,5-dibromo-3,4-dihexylthiophene (dibromo-DHT)** (362 mg, 0.9 mmol, 1 eqv.) was put in a 100 ml flask together with **KOAc** (519 mg, 5.3 mmol, 6 eqv.), **Bpin-Bpin** (538 mg, 2.1 mmol, 2.4 eqv.) and the catalyst **$Pd(ddpf)Cl_2$** (65 mg, 0.08 mmol, 0.09 eqv.) under inert conditions. The mixture was again flushed with **nitrogen**

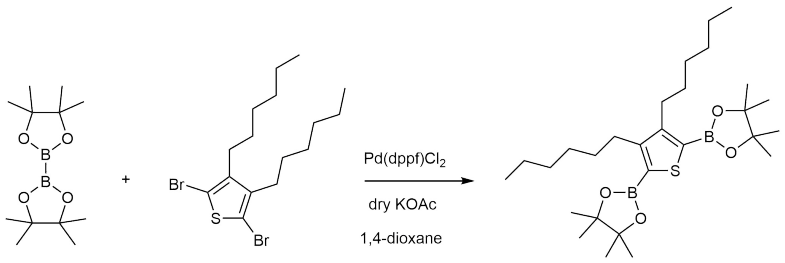

Figure 15: Reaction scheme for the synthesis of Bpin-DHT-Bpin , synthesis approach 2)

Table 7: Masses used for the Synthesis of PMI-DHT-PMI, synthesis approach 2

Name	Mass / mg	Volume / ml	Amount of Substance / mmol	Eqv.
Dibromo-DHT	362	-	0.9	1
Bpin-Bpin	538	-	2.1	2.4
$Pd(dppf)Cl_2$	65	-	0.08	0.09
KOAc	519	-	5.3	6
Dry 1,4-dioxane	-	12	-	-

three times for 20 minutes before adding **dry dioxane** (12 ml). The solution was stirred at 80-90°C under nitrogen flow. Within one hour the mixture turned dark red and the reaction was held over night. The TLC under UV-light showed that the starting material did not react fully, but that two products were formed. After evaporating the **dioxane** and washing it with **CH** and a silica gel filtration was done. A NMR measurement was done and showed that the product was **2,5-dihydrogen-3,4-dihexylthiophene**, comparing with Banishoeib et al. . [49]

Synthesis Approach 3

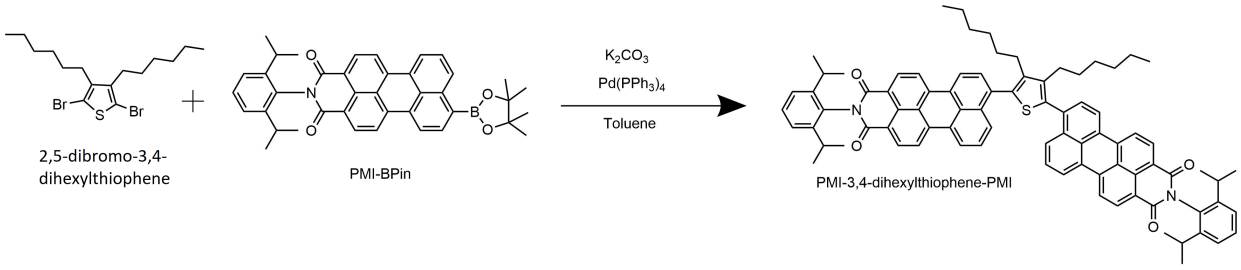

Figure 16: Reaction scheme for the synthesis of PMI-DHT-PMI, synthesis approach 3

The reaction was carried out by Matīss Reinfelds. The synthesis approach was equal to the synthesis of **PMI-3HT-PMI**, using the masses shown in Table 8 and following the reaction scheme shown in Figure 16. The extraction was also done by Matīss Reinfelds, as described in section 4.2.1.

The purification was done by column chromatography, using **CH** and **EA** as eluent (starting from 10% **EA** and increasing to 25% **EA** content). The purity and the structure were

Table 8: Masses used for the Synthesis of PMI-DHT-PMI, synthesis appraoch 3

Name	Mass / mg	Volume / ml	Amount of Substance / mmol	Eqv.
Dibromo-DHT	225	-	0.6	1
PMI-Bpin	734	-	1.2	2.2
$Pd(PPh_3)_4$	0.14	-	0.0001	0.0002
K_2CO_3, 1M	-	15	-	-
Aliquat 336	-	2-3 drops	-	-
Toluene	-	90	-	-

verified with NMR-spectroscopy and can be found in section 6 and was compared with [49].

Yield: 174 mg (0.14 mmol, 26%), dark orange powder, $C_{84}H_{78}N_2O_4S$ (1211.62 g/mol)

^{1}H-NMR (500 MHz, $CDCl_3$) δ = 8.70 - 8.68 (d, 4H, $^3J_{HH}$= 7.00 Hz), 8.55 - 8.49 (m, 8H), 8.07 - 8.05 (d, 2H, $^3J_{HH}$= 8.36 Hz), 7.81 - 7.80 (d, 2H, $^3J_{HH}$= 8.17 Hz), 7.73 - 7.70 (t, 2H, $^3J_{HH}$= 8.01 Hz), 7.51 - 7.48 (t, 2H, $^3J_{HH}$= 7.75 Hz), 7.36 - 7.35 (d, 4H, $^3J_{HH}$= 7.91 Hz), 2.83 - 2.75 (sept, 4H, $^3J_{HH}$= 6.86 Hz), 2.55 (s, 3H), 1.48 - 1.42 (quint, 4H,$^3J_{HH}$= 7.61 Hz), 1.21 - 1.19 (d, 25H, $^3J_{HH}$= 6.83 Hz), 1.13 - 1.07 (m,11H), 0.75 - 0.72 (t, 6H, $^3J_{HH}$= 7.16 Hz)

FT-IR $\bar{\nu}$ (cm^{-1}): 2924, 2860, **1697, 1655 (OCNCO imide)**, 1577, 1353, 1459, 1242, 1183, 808, 751

4.2.4 Characterization Methodology

Thin Layer Chromatography, TLC

The completion of the reactions as well as the purification processes were controlled using TLC. The TLC was done on silica gel 60 plates (Aluminium sheets, purchased from Merck). The products and side products were visible. The eluent used was **CH+EA, 3+1** if not otherwise mentioned.

Column Chromatography

The column chromatography was done using the Biotage Selekt Flash Chromatography. The eluents were **CH** and **EA** for both acceptor materials and the concentration of **EA** was slowly increased from 10% to 25%.

Nuclear Magenetic Resonance (NMR) Spectroscopy

The NMR-measurements were carried out using the following device:
Bruker Advance III spectrometer, 300MHz with an auto sampler for the first measurements
Varian Inova 500, 500 MHz, Oxford Instruments for more precise measurements, carried out by Petra Kaschnitz.

Additional NMR experiments were carried out to approve the chemical structure, i.e. ^{13}C, COSY, HSQC. The ^{1}H NMR spectra can be found in section 6. The used solvent was **$CDCl_3$+TMS**, thus the spectra were referenced against the TMS peak.

Thermogravimetric Analysis, TGA

The TGA measurements were undertaken by Josefine Hobisch on the STA 449C, Netzsch. The measurement was done using a flow rate of 50 ml/min, a heating rate of 10 K/min, a temperature range from 20 - 550 °C and Helium as the protective gas. The sample holder was an aluminium pan.

UV-vis Spectroscopy

The absorption spectra were determined using the spectrometer "UV-1800", Shimadzu. For both linker materials the procedure was as follows:
Three stock solutions were prepared with slightly more than 1 mg diluted in 10 ml **$CHCl_3$**. 1 ml of these solutions was then diluted in 9 ml **$CHCl_3$**. 2 ml of the diluted solutions were mixed with 2 ml **$CHCl_3$**. From the latter, again 2 ml were diluted in 2 ml **$CHCl_3$**.
Using the obtained absorption spectra, the absorption coefficient and the band gap were determined.

Fluorescence Spectroscopy

The measurements were taken together with Matīss Reinfelds and Tobias Burger. First, measurements were undertaken on the UV-Visible Spectrophotometer Cary 50 Conc, Varian to ensure an absorption maximum below 0.10. The measurement settings were as follows: Wavelength range: 500 nm - 900 nm; Slit Width: 1 nm; Scan Speed 70 nm/s

Then the fluorescence measurements were undertaken on the FluoroLog 3 spectrofluorometer, Horiba Scientific Jobin Yvon using the photomultiplier R2658, Hamamatsu. The measurements setttings were as follows: Wavelength range: 500 nm - 850 nm; Slit Width: 4 nm; Excitation Wavelength: 485 nm.

Fluoreszenzorange in **$CHCl_3$** was used as reference material (3 measurements). Three samples were prepared for both acceptor materials by dissolving in **$CHCl_3$** until the absorption maximum was beneath 0.1.

Fourier Transformed Infrared (FT-IR) Spectroscopy

The measurements were undertaken on the Bruker Alpha FT-IR spectrometer with an ATR-IR top unit, using the software Opus. The powder samples were measured by putting them onto the detector and increasing the density by pressing the top crystal onto the sample. The settings can be found in Table 9.

Table 9: FT-IR measurement settings

R / cm-1	4
Background Scans	24
Probe	48
Range / cm-1	4000 - 400

4.3 Organic Photovoltaics

4.3.1 General Methods

Table 10: Chemicals and Materials used for construction of the solar cells.

Chemical	Supplier	Purity grade
2-methoxyethanol	Sigma Aldrich	99.8%
2-propanol	Carl Roth	$\geq$ 99.8%
Chlorobenzene, CB	Sigma Aldrich	99.8%
Ethanolamine	Sigma Aldrich	$\geq$ 99.9%
ITO coated on glass substrate, 15x15x0.1mm	Lumtec	-
Molybdenum oxide, MoO_3	Sigma Aldrich	99.98%
PBDB-T	One Material	-
Silver, Ag	Kurt J. Lesker Company	99.999%
Zinc acetate dihydrate, $ZnAc{\cdot}H_2O$	Emsure	99.5%

The glass-substrate with an ITO-layer, as well as the donor material PBDB-T were purchased from a commercial resource. The two acceptor-materials were mixed with PBDB-T in varying ratios (donor-to-acceptor ratio 1:1 / 2:3 / 3:2).

Table 11: Devices used for the construction of the solar cells

Device	**Manufacturer**
Ultrasonic Cleaner	VWR
Plasma etcher Femto	Diener Electronics
Glove box: LabMaster dp	MBraun
Spin coater: WS-650MZ-23NPPB	Laurel Technologies
Thermal Evaporator: SQM-160	Inficon

The general construction was done as follows:
First the donor and the acceptor were weighed in in different flasks and mixed with the solvent (chlorobenzene (CB), donor: 20 μl per substrate + 30 μl loss, acceptor: 20 μl per substrate + 60 μl loss). The donor and the acceptor mixtures were stirred for 15 minutes at a temperature of 50°C.

The ITO-coated substrates were labelled on the right upper corner of the non-conductive side (=glass side) and subsequently cleaned with distilled water and acetone.
Afterwards, the substrates were cleaned in an isopropanol bath using Ultrasonication (40°C, 60 minutes). Then the glass substrates were dried with nitrogen and plasma-etched for 3 minutes using oxygen plasma.

The next step was spin-coating the ZnO layer onto the ITO-coating (spin-coater settings see Table 12) with a subsequent annealing step (T=150°C, t=15 min). The ZnO solution was prepared by Bettina Schweda: The first step was weighing in **ZnAc*H_2O** (506 mg), **2-methoxyethanol** (5 ml) and **ethanolamine** (150 μl) under inert conditions. Then the solution was stirred over night under ambient conditions. Then the solution was further stirred under inert conditions.

Table 12: General Spin-Coater settings;
Rot. Speed ... Rotational Speed, Acc. ... Acceleration

Material	Step	Volume / μl	Time / s	Rot. Speed / rpm	Acc. / rpm/s
ZnO	1/1	35	30	4000	2000
D-A mixture	1/2	20	60	various	500
	2/2	-	5	4000	4000

Afterwards, the necessary acceptor mixture was transferred to the donor mixture and the solution was stirred for 15 minutes at 80°C and then stirred over night at room temperature. Then the donor-acceptor mixture was spin-coated on top (varying rotational speeds), followed by cutting the electrode spacings free with a knife. Then a MoO_3 layer and then the silver electrode were evaporated on top using shadow masks under minimum vacuum conditions of $1x10^{-5}$ (device settings see Table 13).

Table 13: Thermal Evaporator Settings

Material	Thickness / nm	Deposition rate / Å/s	Density / g/cm^3	Z-factor	Tooling
MoO_3	10	0.1	4.70	1.000	50
Ag	100	1.0-1.2	10.50	0.529	37

The J-V-curves were measured (10ms measurement time, light intensity = 100 mW/cm^2) and the best solar cells were measured again after 10 minutes of light soaking. Furthermore, the thickness of the active layer was measured. Further details on the characterization can be found in section 4.3.2.

4.3.2 Solar Cell Characterization

J-V measurements

The J-V characteristics were measured with light exposure of 100 mW/cm^2 and without light exposure using Dedolight DEB400D lamp. Keithley 2400 SourceMeter and LabView were used for the measurements. The settings for the measurement can be found in Table 14. The active area of the solar cells is 0.070225 cm^2. The resulting V_{OC}, J_{SC}. FF and PCE values were averaged, including only the five best cells. The light-soaking effect was measured for the best cells (10 minutes light exposure).

Table 14: J-V measurement settings

Start / mV	End / mV	Compliance / mA	Number of Points / 100	Overwrite Max. Compliance / mA	Delay / ms	Step Widths / V
1500	-500	100	100	500	100	-0.02

Layer thickness determination

The first step was to scrape away a thin line of the active layer of the solar cells with a blade. Then the layer thickness was measured with a contact profilometer DektaXT from Bruker on three different spots and subsequently averaged.

Light Microscopy

Light microscopy pictures were taken of the active layer with the microscope BX80, Olympus and a connected camera. The pictures were taken in different magnifications (50x, 100x, 200x, 500x, 1000x) and used for a qualitative evaluation of the film quality.

External Quantum Efficiency, EQE

The External Quantum Efficiency was measured for the best cells. The measurement was taken using a xenon lamp (LPS210-U, Amko). The light was going through a monochromator (Multimode 4-AT monochromator, Amko) and the incident photon-to current efficiency was measured using Keithley 2400 SourceMeter. The solar cell was put into a measure box under inert conditions, the EQE measurement was held under normal conditions. Although the oxygen exposure during the measurement was very low due to the used measurement box, a complete prevention of oxygen exposure was not achieved. The measurement was taken in a wavelength range from 350 nm to 900 nm.

Maximum Power Point Tracking, MPP

The Maximum Power Point Tracking was done to observe on one hand the light-soaking effects and on the other hand the stability of the PCE over time. The measurement was done with a light exposure of 100 mW/cm^2 using Dedolight DEB400D lamp. Keithley 2400 SourceMeter and LabView (mpp.vi) were used. The settings for the measurement can be found in Table 15. The active area of the solar cells is 0.070225 cm^2.

Table 15: Settings for the Maximum Power Point Tracking Measurement

Loop time / ms	MPP / mV	Lightgain / mW/cm^2
5000	0.5	293000

UV-vis Spectroscopy

The absorption spectra was determined using the spectrometer "UV-1800", Shimadzu. For both acceptor materials and the donor material the procedure was as follows:
A 10 mg/ml solution in CB was done for each acceptor material, the donor material and

for the acceptor-donor mixture for both acceptor materials (ratio 1:1). The glass substrates were cleaned using acetone, followed by plasma etching (3 minutes, oxygen plasma). Then the solutions were spin-coated on top of the glass substrates. The UV-vis spectra were recorded using a clean glass substrate as reference from 400 to 700 nm.

5 Results and Discussion

5.1 Results based on Density Functional Theory

The density functional theory (DFT) calculations were done for both acceptor materials. Since the imide groups and the hexyl-chains do not contribute to the optical properties of the molecules, both were substituted with methyl groups. For control purposes, one structure was additionally calculated with the hexyl-chain (PMI-3HT-hex-PMI). Furthermore, the calculations were done for the flipped and non-flipped structures, as depicted for PMI-3HT-PMI in Figure 17. The first step, was the geometrical optimization. Subsequently, the dihedral angles were measured, as depicted in Figure 18. Taking a look at Table 16, one can see that there are only slight differences between the dihedral angles of PMI-3HT-PMI, flipped and PMI-3HT-hex-PMI, flipped, as expected. Furthermore, especially the side with the hexyl-chain (left angle) shows great differences between the flipped and non-flipped state. Generally, the left and the right angle are different for the flipped and the non-flipped state of PMI-3HT-PMI. On the other hand, the flipped state of PMI-DHT-PMI is symmetrical, while the non-flipped state shows a difference between the left and the right angle in the same order as PMI-3HT-PMI. Furthermore, the difference between angles of the flipped and non-flipped state is more pronounced for the left angle of PMI-DHT-PMI. Comparing PMI-3HT-PMI and PMI-DHT-PMI, both acceptor molecules show dihedral angles of equal magnitude.

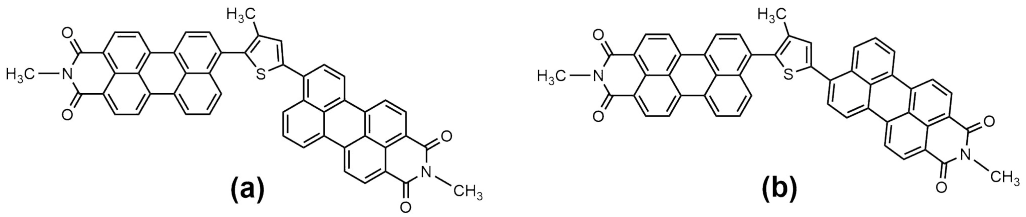

Figure 17: Illustration of the (a) non-flipped and (b) flipped molecules using PMI-3HT-PMI as an example

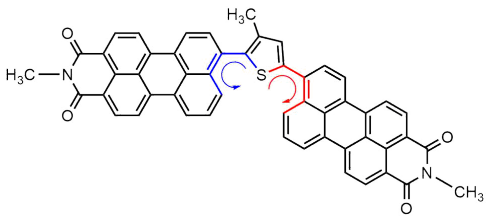

Figure 18: Illustration of the dihedral angles measured using PMI-3HT-PMI as an example

The next step was the calculation of the corresponding HOMO and LUMO levels, as well as of the optical band gap and the absorption maximum wavelength. The results are summarized in Table 17. Comparing the flipped and non-flipped states of both acceptor materials respectively, they show similar results in general. Furthermore, both acceptor

Table 16: Dihedral angels for all calculated structures

Molecule	Angle in gas phase, left / °	Angle in gas phase, right / °
PMI-3HT-PMI, non-flipped	58.5	53.4
PMI-3HT-PMI, flipped	68.7	54.0
PMI-3HT-hex-PMI, flipped	66.8	53.9
PMI-DHT-PMI, non-flipped	60.2	68.5
PMI-DHT-PMI, flipped	69.5	69.5

molecules show greater oscillator strength (f) and wavelengths (λ^{opt}) but lower optical band gaps ($E_g{}^{opt}$) for the flipped state. Moreover, the difference between the flipped and non-flipped states is significant, which is assumed to be due to the different molecular geometry. Additionally, it can be seen in Table 17, that the simplification of the molecules by substituting the hexyl-chains did not lead to significant changes in the results. Furthermore, there are only slight differences between the two different acceptor materials as well, which supports once more the independence of optical characteristics on introduced hexyl-chains. This can also be seen by comparing Figure 19 and 20: The flipped PMI-3HT-PMI and the flipped PMI-3HT-hex-PMI show similar behaviour for the HOMO-LUMO transition. However, comparing the non-flipped and flipped PMI-3HT-PMI, one can see that the non-flipped state shows charge transfer from the thiophene unit to the PMI units, while in case of the flipped PMI-3HT-PMI charge is remaining more prominently on the sulfur atom of the thiophene unit. This behaviour can also be observed for PMI-DHT-PMI.

Furthermore, the graphical representation of the HOMO and LUMO levels for all calculated molecules as well as for the donor material (PBDB-T), the two interlayers (ZnO, MoO_3) and the two electrodes (ITO, Ag) can be found in Figure 22. The figure depicts the good matching between the energy levels of the used materials.

Table 17: Results of the DFT-based calculations regarding the optical properties of the acceptor materials

Molecule	HOMO / eV	LUMO / eV	$E_g{}^{opt}$ / eV	λ^{opt} / nm	f
PMI-3HT-PMI,non-flipped	3.32	5.74	2.15	577	1.00
PMI-3HT-PMI,flipped	3.47	5.48	1.86	668	1.62
PMI-3HT-hex-PMI,flipped	3.44	5.46	1.86	667	1.60
PMI-DHT-PMI,non-flipped	3.29	5.76	2.22	560	0.96
PMI-DHT-PMI,flipped	3.42	5.45	1.86	666	1.50

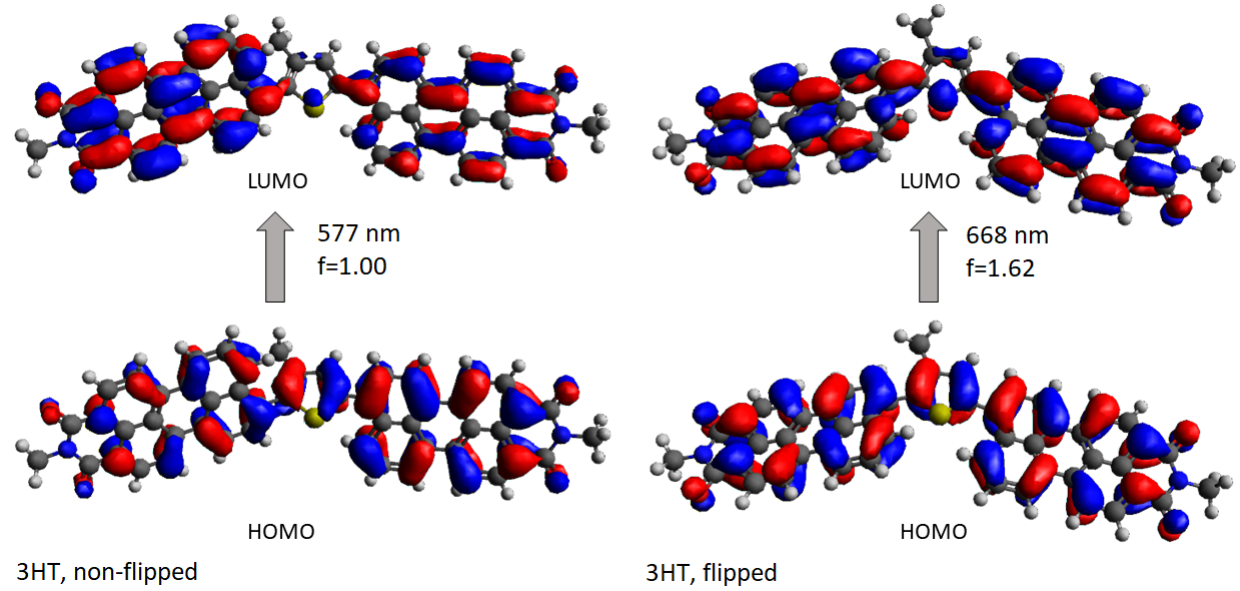

Figure 19: Calculated HOMO-LUMO transition for PMI-3HT-PMI, left: non-flipped, right: flipped

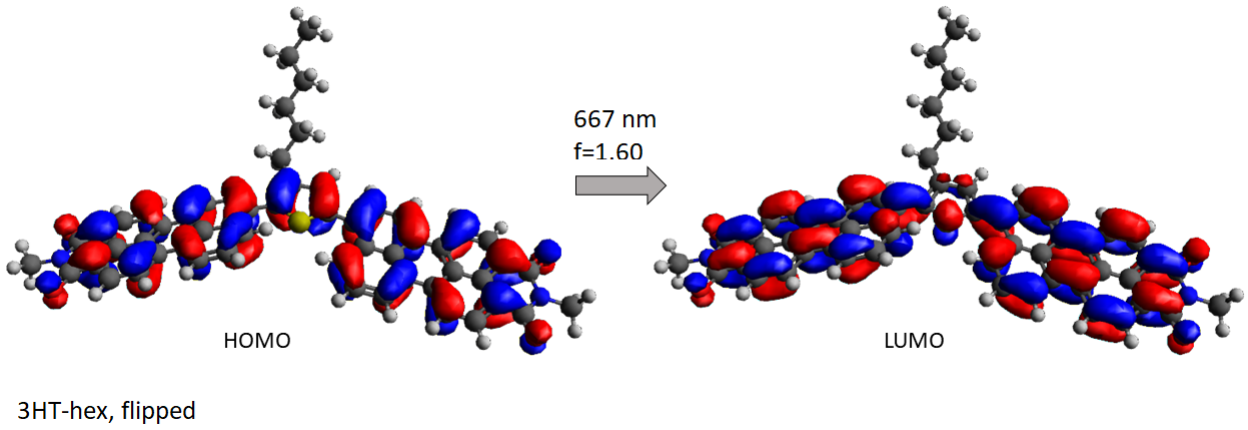

Figure 20: Calculated HOMO-LUMO transition for PMI-3HT-hex-PMI with hexylchain, flipped

5.2 Synthesis of PMI-based Acceptors

In Figure 23 the different synthesis steps are depicted.

General Synthesis Route for the acceptor materials

The principal synthesis route was for both acceptor materials the same, as illustrated in **reaction schemes 3** and **4** in Figure 23.

The linker molecules (**2,5-dibromine-3-hexyl-thiophene**; **2,5-dibromine-3,4-dihexyl-thiophene**) were used in a Suzuki-Coupling reaction, shown in Figure 24.

Therefore, the linker molecule was mixed with **PMI-Bpin** and **K_2CO_3** as a base to activate the transmetallation of the boronic **PMI-Bpin**. **Toluene** was used as a solvent. **$Pd(PPh_3)_4$** was added to the mixture under inert conditions to intervene oxidation and prevent inactivation of the catalyst. [46]

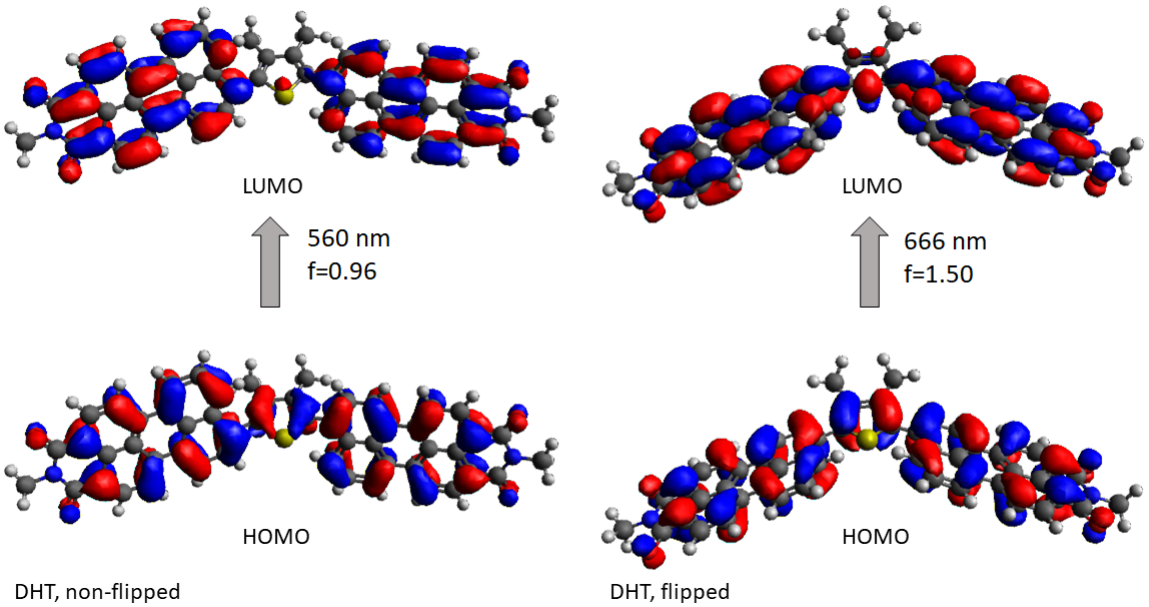

Figure 21: Calculated HOMO-LUMO transition for PMI-DHT-PMI, left: non-flipped, right: flipped

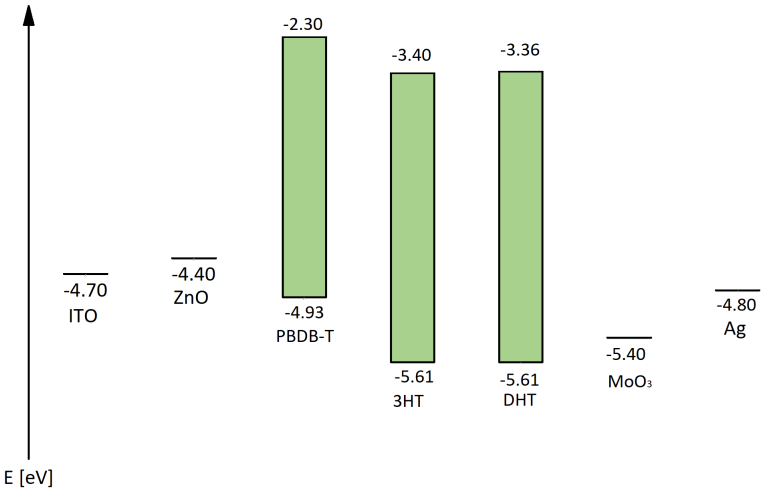

Figure 22: Comparison of the energy levels of all materials used

The products were then extracted using $\mathbf{H_2O}_{dist}$ and **DCM** to remove the base. Purification was done via column chromatography, recrystallization and precipitation. The purity and the structure were verified via NMR spectroscopy. The reactions were straight forward and are described in detail in section 4.2.1.

5.2.1 PMI-3HT-PMI

A detailed description of the synthesis can be found in section 4.2.2.

The purification of remained product from Sanela Alibegic turned out to be difficult due to the appearance of a by-product, which is believed to be PMI-PMI and showed almost

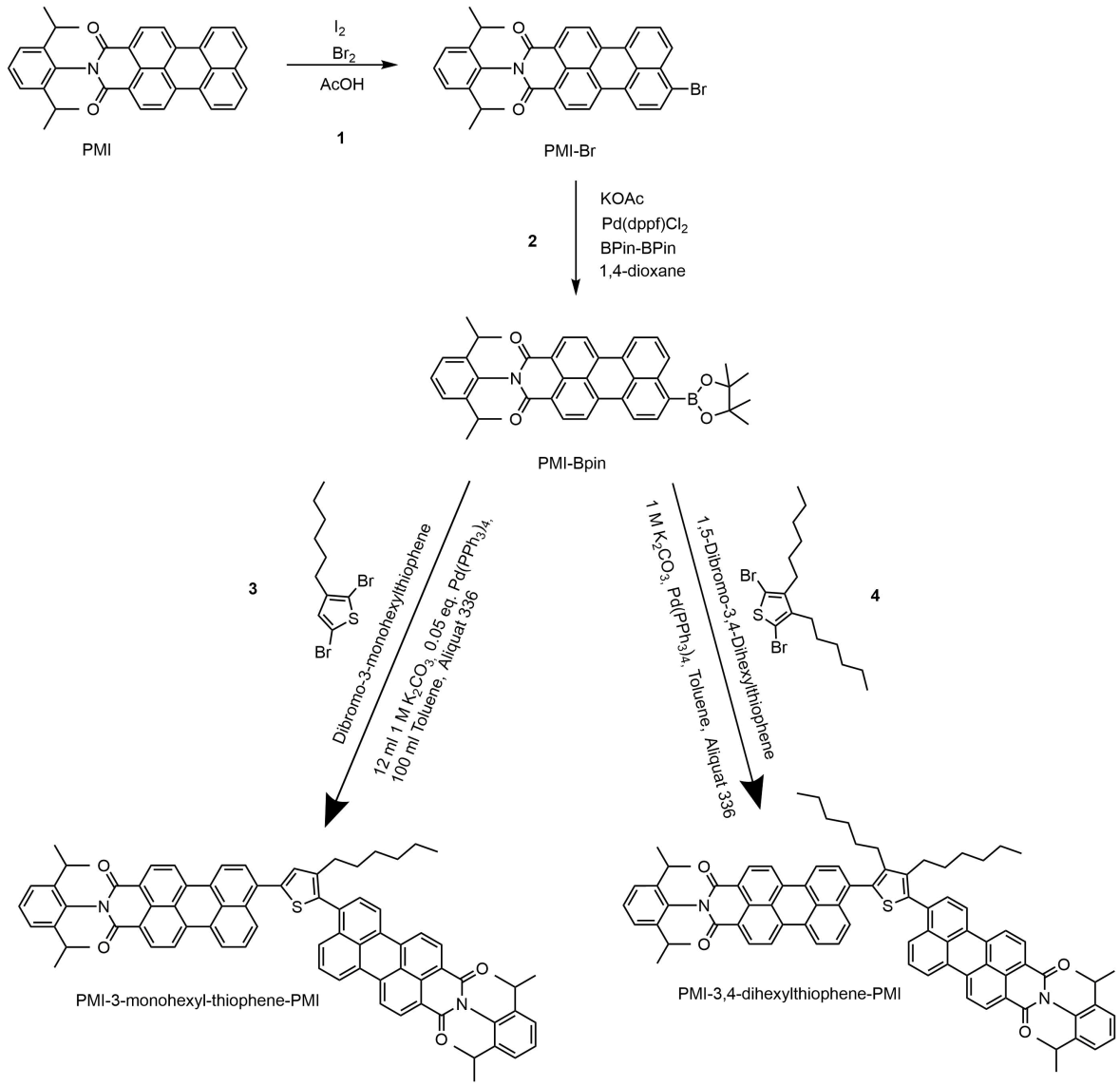

Figure 23: General Synthesis procedure
1 - PMI-Br synthesis route, **2** - PMI-Bpin synthesis route, **3** - PMI-3HT-PMI synthesis route, **4** - PMI-DHT-PMI synthesis route

equal R_f value (see Figure 25). This supported the approach to try a different synthesis route. Different synthesis approaches were done for producing PMI-DHT-PMI, and the best working approach with easy purification due to very little by-products was applied also for PMI-3HT-PMI due to their similar structure.

During the synthesis, 0.25 eqv. of **PMI-Bpin** were added every 20-25 minutes after ensuring full conversion to prevent the formation of the by-product (PMI-PMI). Although there were less side-products compared to the remaining product that was only purified, purification was still challenging.

The first approach was trying different eluents to separate the product from the by-products. The best eluent was **CH+EA, 3+1**, but still multiple column chromatographies were necessary.

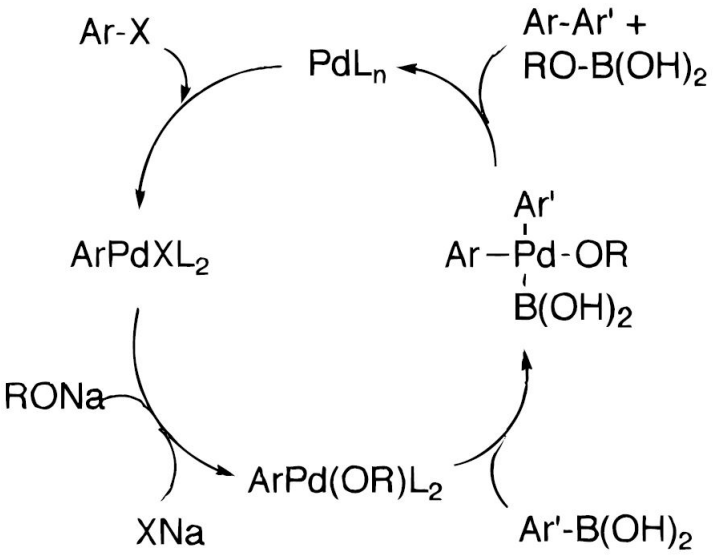

Figure 24: Suzuki Coupling Mechanism, Reprinted with permission from [46]. Copyright (1996) American Chemical Society

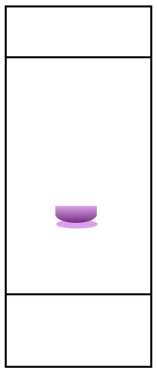

Figure 25: Illustration of the TLC for PMI-3HT-PMI, including the product (upper spot) and the by-product (spot below)

Another attempt was recrystallization using **EA** as solvent. Since this did not improve the quality as hoped, the anti-solvent **CH** was added. This approach did remove parts of the difficult side-product.

Building a precipitate using **DCM** and **MeOH** did also increase quality only partially.

5.2.2 PMI-DHT-PMI

A detailed description of all synthesis approaches can be found in section 4.2.3.

Due to the faced difficulties for PMI-3HT-PMI regarding the amount of by-products and the similarity to the chemical structure between both linker materials, different synthesis routes were tried for PMI-DHT-PMI.

Synthesis Approach 1

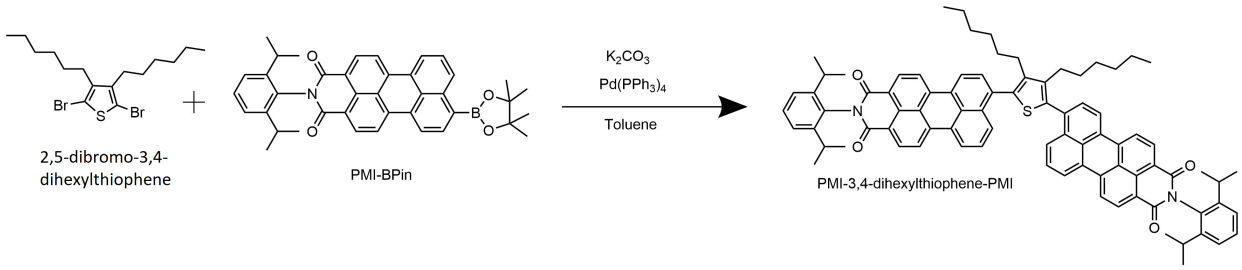

Figure 26: Reaction scheme for the synthesis of PMI-DHT-PMI, synthesis approach 1

The first approach (see Figure 26) was to put the educts **dibromo-DHT**, **K_2CO_3**, **Aliquat 336**, **toluene** and **PMI-Bpin** in a flask. After ensuring inert conditions via flushing the flask with nitrogen, the catalyst, **$Pd(PPh_3)_4$**, was added. The solution was reacting over night under a temperature of 80-90°C under inert conditions until full conversion was reached. After extraction, the TLC showed many by-products. During purification it turned out, that the reaction did not result in sufficient amount of the desired product. This suggested, that adding **PMI-Bpin** in excess favours conversion to the side-product **PMI-PMI** more than the reaction to the desired product. Thus, another approach was tried.

Synthesis Approach 2

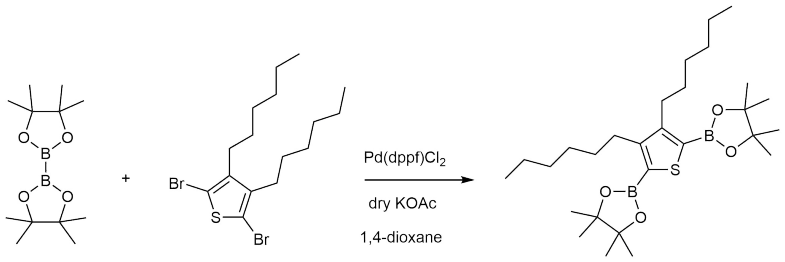

Figure 27: Reaction scheme for the synthesis of Bpin-DHT-Bpin, synthesis approach 2

The next approach was to first convert **dibromo-DHT** to **bpin-DHT-bpin**, as depicted in Figure 27, and then utilize PMI-Br as a coupling partner to obtain the desired product. Therefore, **dibromo-DHT**, **KOAc**, **Bpin-Bpin** and the catalyst **$Pd(ddpf)Cl_2$** were weighed in in a flask under inert conditions. After flushing the mixture with **nitrogen** three times to ensure that any remaining oxygen in the flask can be excluded, **dry dioxane** was added. Within one hour of stirring the solution at 80-90°C, the solution turned dark red. The reaction was continued over night. The next day, the TLC under UV-light showed no full conversion of the starting material. Nonetheless, the solution was distilled via rotary-evaporation and subsequently washed with **CH**. A silica gel filtration was done and the

NMR spectra of the product showed the reaction to **DHT** instead of the desired product, comparing with Banishoeib et. al. [49] It has been reported, that the use of heterocyclic, electron-rich boronates like Bpin-thiophene promotes protodeboronation. [50] Although in this reaction approach Bpin-Bpin was used and not Bpin-thiophene, the educt dibromo-DHT and Bpin-Bpin probably built the intermediate product Bpin-DHT-Bpin followed by protodeboronation to 3,4-dihexylthiophene.

Synthesis Approach 3

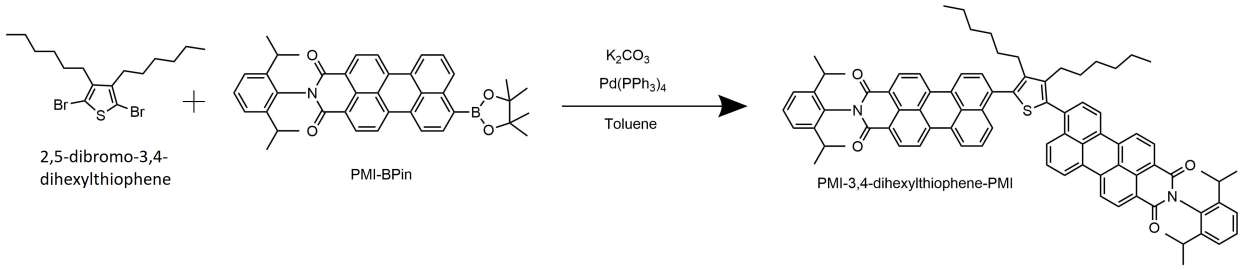

Figure 28: Reaction scheme for the synthesis of PMI-DHT-PMI, synthesis approach 3

The third approach (see Figure 28) was in principal the same as the first approach, but this time only 0.25 eqv. of **PMI-Bpin** was added to the reaction until full conversion was reached. After full conversion, again 0.25 eqv. were added and this procedure was repeated until the full amount of **PMI-Bpin** was added. However, this reaction was done by Matīss Reinfelds and is described in more detail in section 4.2.3. The side products were less, thus strengthening the assumption that excess of **PMI-Bpin** favours the reaction of undesired by-products.

5.3 Compound Characterization

Thermogravimetric Analysis, TGA

The thermal stability was measured for both acceptor materials by Josefine Hobisch using thermogravimetric analysis, as can be seen in Figure 29. The blue line depicts the mass loss as a function of temperature for PMI-DHT-PMI and the red line illustrates the mass loss for PMI-3HT-PMI.

PMI-3HT-PMI started to slowly lose mass at 94°C suggesting that there was still solvent remaining in the sample. The total mass loss was 26.7% at 540°C. PMI-DHT-PMI on the other hand showed a rather sudden start of weight loss at 428°C. At the end of the measurement at 540°C a mass loss of 25.1% was reached.

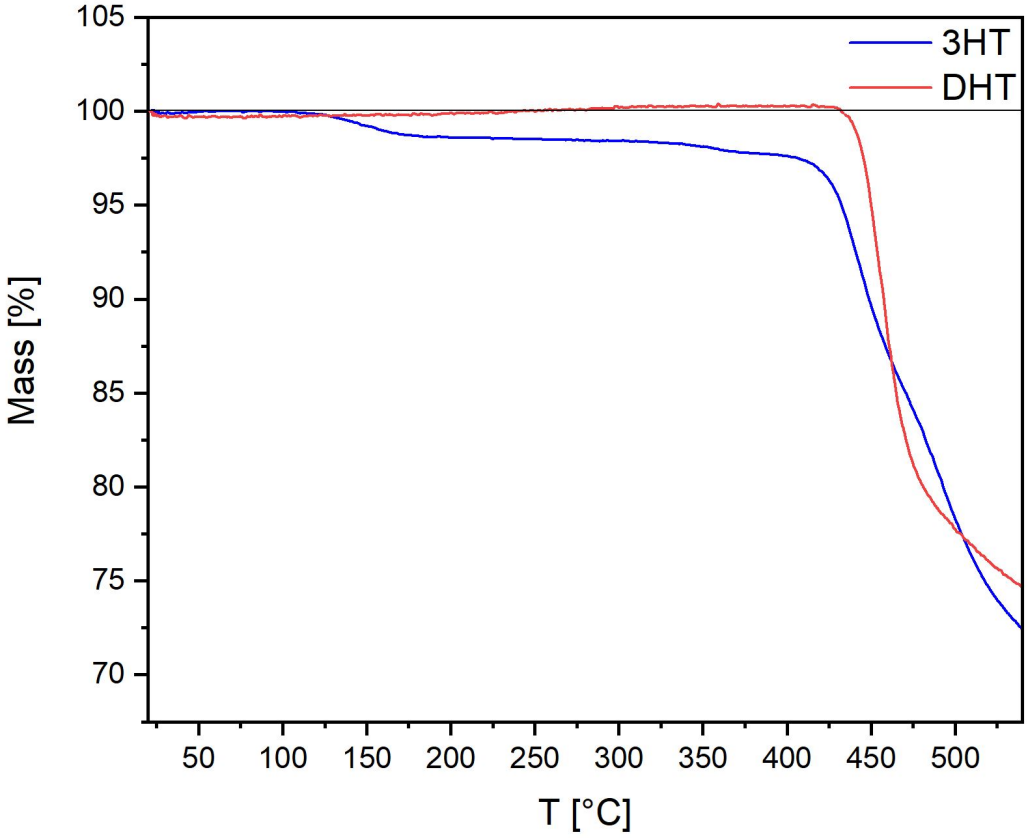

Figure 29: TGA measurement of PMI-3HT-PMI (red, 3HT) and PMI-DHT-PMI (blue, DHT)

UV-vis Spectroscopy in solution

The absorption was measured for both acceptor materials in solutions of **$CHCl_3$**, as can be seen in Figure 30. Furthermore, the molar absorption coefficients and the optical band gap were determined:

PMI-3HT-PMI showed an absorption maximum at 530 nm, a molar absorption coefficient of $8.8 \cdot 10^4$ $M^{-1}cm^{-1}$ and a optical band gap of 586 nm (2.12 eV). PMI-DHT-PMI had the absorption maximum at 529 nm, the molar coefficient was $11.3 \cdot 10^4$ $M^{-1}cm^{-1}$ and the optical band gap was 567 nm (2.19 eV). Furthermore, both acceptor material showed a local maximum at 488 nm, although it is more pronounced for PMI-DHT-PMI.

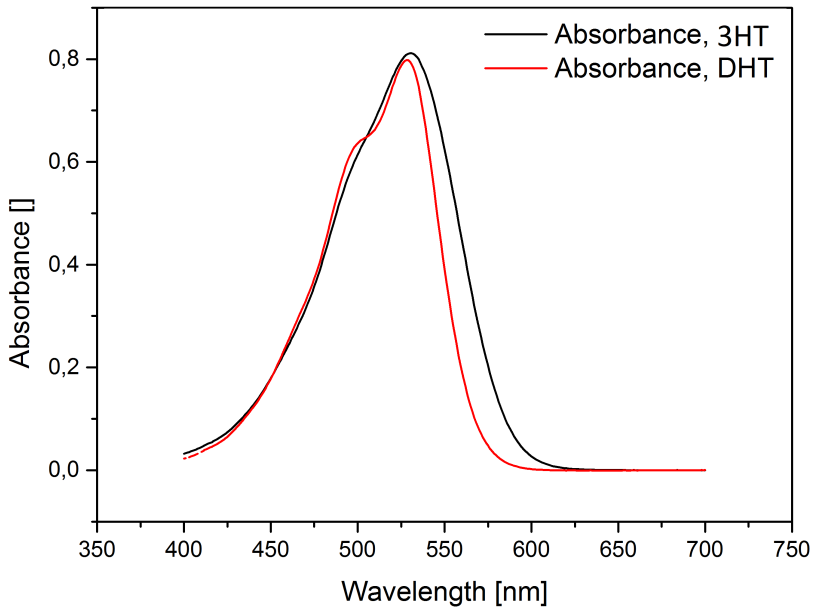

Figure 30: UV-vis absorbance spectra, PMI-3HT-PMI and PMI-DHT-PMI in comparison

Fluorescence Spectroscopy

The fluorescence spectra can be seen in Figure 31. The emission maxima were at 614 nm and 590 nm for PMI-3HT-PMI and PMI-DHT-PMI, respectively. Considering the absorption maxima (PMI-3HT-PMI: 530 nm, PMI-DHT-PMI: 529 nm), the determined Stokes shifts were 84 nm (PMI-3HT-PMI) and 61 nm (PMI-DHT-PMI). The fluorescence quantum yields were determined to be Φ=20%(PMI-3HT-PMI) and Φ=29% (PMI-DHT-PMI), using Fluoreszenzorange as a reference (Φ=98%).

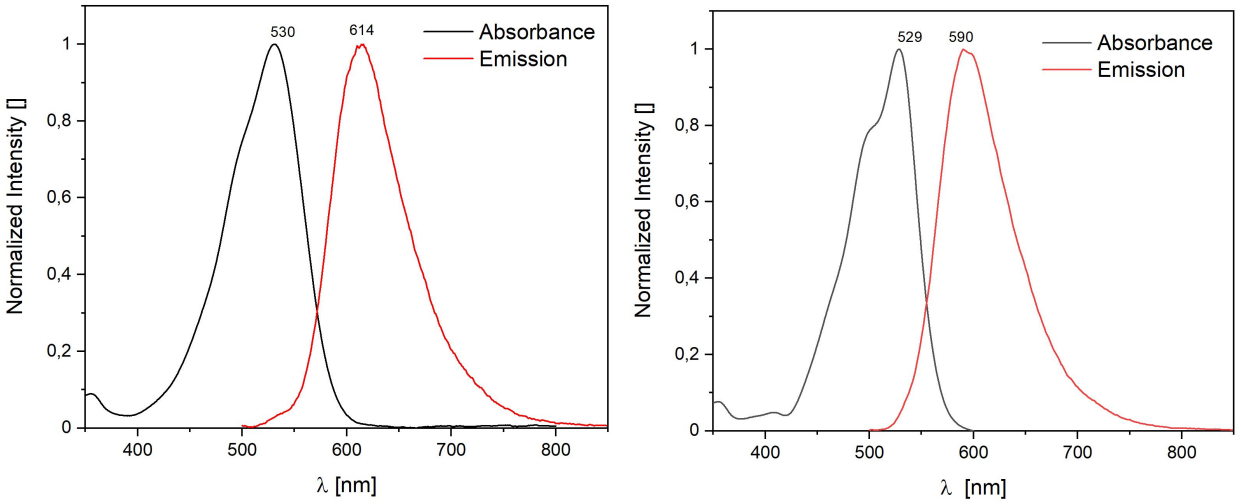

(a) PMI-3HT-PMI (b) PMI-DHT-PMI

Figure 31: Absorbance and Emission spectra of both acceptor materials

UV-vis Spectroscopy of the layers

The absorbance spectra of the layers of the two acceptors materials, as well as the donor material (PBDB-T) and 1:1 mixtures of each acceptor material and the donor were measured before and after heat treatment (t=10 minutes, T=160 °C). The results are shown in Figure 32. The absorption spectra for the acceptor materials in thin films and the absorption spectra in solution show a similar shape. However, while the thin film of PMI-3HT-PMI is not shifted compared to the UV-vis spectra in solution of PMI-3HT-PMI and shows an absorption maximum at 530nm, the PMI-DHT-PMI is slightly red-shifted to 533 nm. Furthermore, comparing the tempered and not tempered samples, one can see slight changes in the absorption spectra as well:

As already Liang et al. observed, thermal annealing yields in improved crystallinity of the donor material PBDB-T. [51] This enhancement in crystallinity results in a red-shift of the maximum peak from 623 nm to 628 nm. Furthermore, also the absorption spectra of both donor-acceptor mixtures illustrate, that the influence of thermal annealing is stronger for PBDB-T by showing a stronger change of the spectra in the PBDB-T range.

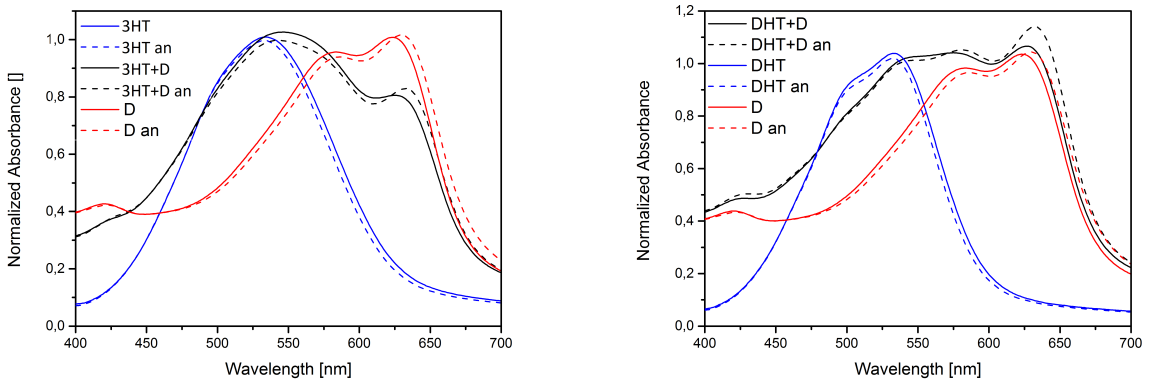

(a) PMI-3HT-PMI

(b) PMI-DHT-PMI

Figure 32: UV-vis absorbance spectra of the annealed (=an) and not annealed layers of both acceptor materials, the donor PBDB-T (=D), and both acceptor-donor mixtures

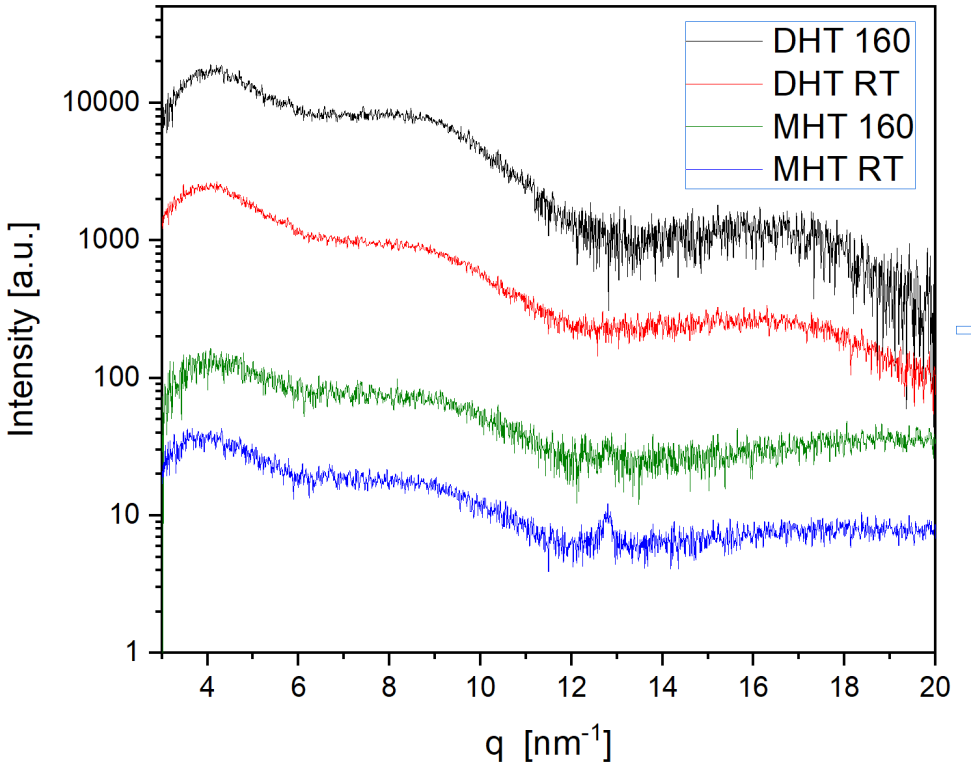

Figure 33: XRD measurements of PMI-3HT-PMI and PMI-DHT-PMI before and after annealing at 160°C for 10 minutes

X-ray diffraction, XRD

The XRD measurements were undertaken by Thomas Rath on drop-casted films before and after thermal annealing (t=10 minutes, T=160°C), as can be seen in Figure 33. Generally, a slight increase of the intensities can be observed for the annealed thin films. Both samples show a peak at 4.1 nm^{-1}. Furthermore, PMI-DHT-PMI depicts another broad peak at about 17 nm, while this peak cannot be clearly seen for PMI-MHT-PMI. This peak was also reported by Weber et al. for perylenemonoimide based acceptor materials using fluorene, silafluorene or carbazole as linker compounds and was correlated with $\pi - \pi$ stacking. [42] On the other hand, PMI-MHT-PMI shows a clear peak for the non-annealed sample at 12.8 nm. All in all, the peaks are slightly more pronounced for PMI-DHT-PMI, suggesting a higher crystallinity. Nonetheless, both samples do not show pronounced crystallinity.

5.4 Organic Photovoltaics

The solar cells were all constructed using PBDB-T as a donor material. For both acceptor materials, the influence of the thickness of the active layer was investigated, as well as the impact of different donor-to-acceptor ratios. Furthermore, two different heat treatments were tried (solvent vapor annealing vs thermal annealing). The stability over time was tested using maximum power point tracking. Lastly, external quantum efficiencies measurements were done.

5.4.1 PMI-3HT-PMI

For practise purposes, the very first experiment was done with not completely pure PMI-3HT-PMI to avoid common mistakes that might occur during the first try with the pure acceptor material. However, the results obtained were the best for the acceptor material PMI-3HT-PMI and can be found in Table 18. First of all, one can notice that the active layer thickness of all assembled solar cells in Table 18 is only 34 to 43 nm, while the best solar cells assembled by Sanela Alibegic showed a layer thickness of 56 nm. [9] For both cases, the active layer thickness is below the ideal thickness of 100 nm. Furthermore, there is a rapid growth of the power conversion efficiency to 1.10 % with a layer thickness of 43 nm compared to the solar cells assembled with 1000 or 1500 rpm and a layer thickness of 36 and 34 nm, respectively. However, the solar cell assembled with a rotational speed of 2500 rpm resulted also in an active layer thickness of 36 nm but in greater power conversion efficiency of 0.95 %. The best solar cell in this experiment gave an open-circuit voltage of 1.01 V, a short-circuit current of 3.13 mA and a fill factor of 35 %.

Table 18: Solar cell characteristics for differing rotational speeds for not fully pure PMI-3HT-PMI with PBDB-T, d:a ratio 1:1, 10 mg/ml
ω...rotational speed, t...thickness

ω **rpm**	**t / nm**	**PCE / %**	$\mathbf{V_{OC}}$ **/ V**	$\mathbf{J_{SC}}$ **/ mA**	**FF / %**
1000	36	0.58 ± 0.02	0.90 ± 0.01	1.57 ± 0.05	41 ± 1
1500	34	0.58 ± 0.50	0.60 ± 0.47	1.74 ± 1.66	45 ± 3
2000	43	1.10 ± 0.08	1.01 ± 0.02	3.13 ± 0.10	35 ± 2
2500	36	0.95 ± 0.13	0.93 ± 0.01	2.82 ± 0.06	36 ± 1

The next attempt was testing different rotational speeds for spin-coating the active layer to find the optimum thickness, using pure PMI-3HT-PMI in a 1:1 donor-to-acceptor ratio. Table 19 shows the results of this experiment. The best power conversion efficiencies were reached for the solar cells with an active layer thickness of 51 to 55 nm. The solar cells within this layer thickness range did not show great performance differences. The best solar cell achieved a power conversion efficiency of 0.87 %, an open-circuit voltage of 0.65 V, a short-circuit current of 3.37 mA and a fill factor of 40 % with a layer thickness of 51 nm. All solar cells with a layer thickness below 63 nm showed a decrease of the power conversion efficiency, the open-circuit voltage and the short-circuit current after

annealing. Since the solar cells were annealed after evaporating MoO_3 and Ag on top of the active layer, it is assumed that the electrode deteriorated the active layer during the annealing step, which results in lower power conversion efficiencies. However, the solar cells with thicker active layers showed slightly increasing power conversion efficiencies. Thus, the active layer was thick enough to sufficiently prevent the deterioration process. Furthermore, light-soaking did not improve the performance of the solar cells in general.

Table 19: Solar cell characteristics for differing rotational speeds for PMI-3HT-PMI with PBDB-T before and after annealing (t=10 minutes, T=160 °C) and light-soaking after annealing (LS, 10 minutes)
d:a ratio 1:1, 15 mg/ml
ω...rotational speed, t...thickness, LS...light-soaking, max...best cell

ω / rpm	t / nm	Annealed?	PCE / %	V_{OC} / V	J_{SC} / mA	FF / %
1000	78 ± 1	No	0.32 ± 0.03	0.62 ± 0.02	1.41 ± 0.10	37 ± 1
		Yes	0.35 ± 0.02	0.44 ± 0.02	1.71 ± 0.09	47 ± 1
1200	71 ± 8	No	0.42 ± 0.10	0.68 ± 0.10	1.83 ± 0.27	34 ± 1
		Yes	0.57 ± 0.03	0.56 ± 0.05	2.29 ± 0.24	45 ± 2
		Yes + LS	0.57 ± 0.04	0.52 ± 0.05	2.29 ± 0.24	45 ± 2
1400	63 ± 4	No	0.58 ± 0.07	0.62 ± 0.04	2.47 ± 0.14	38 ± 1
		Yes	0.46 ± 0.04	0.42 ± 0.02	2.36 ± 0.09	46 ± 1
1600	52 ± 5	No	0.66 ± 0.14	0.60 ± 0.05	2.86 ± 0.18	38 ± 4
		Yes	0.43 ± 0.05	0.38 ± 0.02	2.50 ± 0.14	46 ± 1
1800	52 ± 5	No	0.72 ± 0.09	0.65 ± 0.07	3.08 ± 0.10	36 ± 1
2000	55 ± 12	No	0.68 ± 0.05	0.62 ± 0.04	2.95 ± 0.19	38 ± 1
		Yes	0.49 ± 0.04	0.38 ± 0.03	2.79 ± 0.15	47 ± 1
		Yes + LS	0.45 ± 0.04	0.35 ± 0.03	2.79 ± 0.18	46 ± 1
2200	51 ± 5	No	0.70 ± 0.10	0.58 ± 0.05	3.10 ± 0.17	39 ± 1
		Yes	0.49 ± 0.04	0.38 ± 0.03	2.79 ± 0.15	47 ± 1
		Yes + LS	0.41 ± 0.05	0.34 ± 0.02	2.62 ± 0.121	45 ± 1
2400	52 ± 5	No	0.62 ± 0.16	0.53 ± 0.09	3.12 ± 0.23	37 ± 2
		Yes	0.37 ± 0.10	0.32 ± 0.05	2.62 ± 0.18	43 ± 4
2200	51 ± 5	No, max	0.87	0.65	3.37	40

The next step was to analyze the influence of different donor-to-acceptor ratios on the solar cell performance, as shown in Table 20. Generally, the solar cells with lower acceptor content (3:2 ratio) outperformed those with higher acceptor content (2:3 ratio), which could be due to better phase separation. Furthermore, the rotational speed influenced the active layer thickness significantly in case of a 3:2 ratio while in case of a 2:3 ratio the layer thickness was independent of the rotational speed. However, in both cases, the solar cells performed best with a layer thickness of about 52 nm. The best solar cell with a 3:2 ratio reached a power conversion efficiency of 0.76 %, a open-circuit voltage of 0.59 V and a short circuit current of 2.81 mA with a thickness of 52 nm, while the best solar cell with a 2:3 ratio achieved a power conversion efficiency of 0.67 %, a open-circuit voltage of 0.49 V and a short-circuit current of 3.02 mA with a thickness of 51 nm. Additionally, light-soaking did not change or worsened the performance of solar cells with a 2:3 ratio, while

a slight improvement was observed for solar cells with a 3:2 ratio and a layer thickness of 52 nm.

Table 20: Influence of donor-to-acceptor ratios on the solar cell characteristics using PMI-3HT-PMI as acceptor material and applying an annealing step (T=160 °C, t=10 minutes) d:a ratios 3:2 and 2:3, 15 mg/ml, annealing time: 10 minutes
ω...rotational speed, t...thickness, info...information, max...maximum values reached, LS...light-soaking 10 minutes

d:a ratio	ω **/ rpm**	**t / nm**	**Info**	**PCE / %**	$\mathbf{V_{OC}}$ **/ V**	$\mathbf{J_{SC}}$ **/ mA**	**FF / %**
3:2	1000	78 ± 1		0.34 ± 0.02	0.49 ± 0.02	1.50 ± 0.07	47 ± 1
			LS	0.32 ± 0.03	0.50 ± 0.02	1.44 ± 0.05	45 ± 1
	1400	70 ± 10		0.43 ± 0.01	0.55 ± 0.03	1.83 ± 0.06	43 ± 1
	1800	63 ± 4		0.50 ± 0.04	0.55 ± 0.02	2.13 ± 0.12	42 ± 1
	2200	52 ± 5		0.69 ± 0.05	0.62 ± 0.03	2.65 ± 0.13	42 ± 1
			LS	0.70 ± 0.05	0.59 ± 0.02	2.83 ± 0.12	42 ± 1
2:3	1000	52 ± 1		0.23 ± 0.02	0.44 ± 0.02	1.19 ± 0.09	44 ± 3
			LS	0.23 ± 0.01	0.42 ± 0.02	1.27 ± 0.08	43 ± 2
	1400	55 ± 11		0.43 ± 0.04	0.44 ± 0.02	2.24 ± 0.11	44 ± 1
	1800	51 ± 5		0.58 ± 0.07	0.47 ± 0.03	2.79 ± 0.16	45 ± 1
	2200	52 ± 5		0.54 ± 0.05	0.44 ± 0.02	2.76 ± 0.19	44 ± 1
			LS	0.34 ± 0.28	0.25 ± 0.20	2.10 ± 1.59	66 ± 28
3:2	2200		LS, max	0.76	0.59	2.81	43
2:3	1800		max	0.67	0.49	3.02	45

Another approach was to use solvent vapor annealing instead of thermal annealing. The solvent used was CB and the results can be found in Table 21. In this case the best cell reached a power conversion efficiency of 0.74 %, an open-circuit voltage of 0.73 V and a short-circuit current of 2.17 mA. However, compared to the solar cells with a 3:2 ratio and thermal annealing, the solar cell performance was slightly lower.

Table 21: Influence of solvent vapor annealing (solvent: CB, 160 °C, 10 minutes) on the solar cell characteristics, using PMI-3HT-PMI as acceptor material and a donor-to-acceptor ratio of 3:2.
ω...rotational speed, LS...light-soaking, max...maximum values achieved

ω **/ rpm**	**Info**	**PCE / %**	$\mathbf{V_{OC}}$ **/ V**	$\mathbf{J_{SC}}$ **/ mA**	**FF / %**
1000		0.65 ± 0.07	0.70 ± 0.02	2.01 ± 0.17	46 ± 0.01
	LS	0.59 ± 0.08	0.65 ± 0.02	1.90 ± 0.20	48 ± 1
2200		0.38 ± 0.04	0.54 ± 0.01	1.37 ± 0.10	52 ± 1
	LS	0.40 ± 0.04	0.53 ± 0.02	1.64 ± 0.10	51 ± 1
1000	max	0.74	0.73	2.17	47
2200	max, LS	0.45	0.55	1.64	51 ± 1

The J-V curve of the best cell in Table 19 can be found in Figure 34. The red (light) curve shows a greater incline than the blue (dark) curve in the first quadrant. Furthermore, the red (light) curve shows a constant decrease in the third an fourth quadrant. The short-circuit current in the graph is 2.53 mA/cm^2 and the open-circuit voltage is 0.65 V.

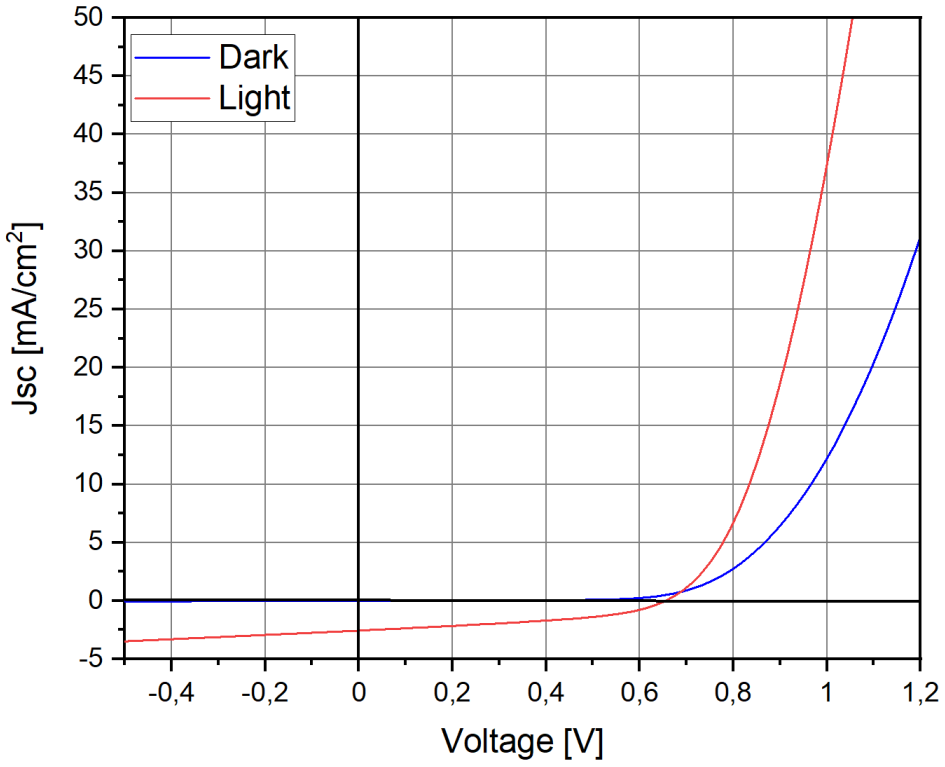

Figure 34: J-V curve for the best cell using PMI-3HT-PMI as acceptor material; donor-to-acceptor ratio 1:1, thermal annealing (t=10 minutes, T=160°C), 15 mg/ml, ω=1800rpm, see Table 19

The maximum power point was tracked over a time of 132 minutes, as can be seen in Figure 35.It can be seen, that the power conversion efficiency is increasing fast in the first 10 minutes. Afterwards, the power conversion efficiency is slightly increasing, followed by a drop after about 60 minutes. Then, the power conversion efficiency is starting to stabilize.

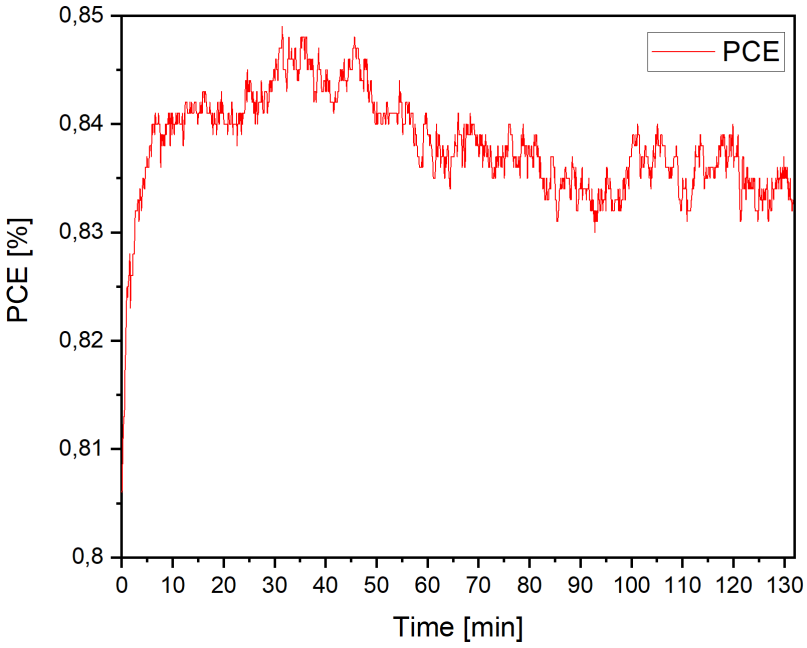

Figure 35: Maximum power point tracking for the solar cells using PMI-3HT-PMI as acceptor material; donor-to-acceptor ratio 1:1, thermal annealing (t=10 minutes, T=160°C), 15 mg/ml, ω=1800 rpm, see Table 19

5.4.2 PMI-DHT-PMI

The first attempt, see Table 22, was to use a donor-to-acceptor ratio of 1:1 and various rotational speeds for spin-coating the active layer. The rotational speed was varied between 1000 and 2400 rpm. The increase of the rotational speed was positively correlated with the PCE, V_{OC} and J_{SC} and negatively correlated with the layer thickness and roughness. As for PMI-3HT-PMI, an active layer of 50 nm resulted in better performance than an active layer of 100 nm. The influence of the annealing temperature on the solar cell characteristics was tested using 2400 rpm due to the achieved results in the prior mentioned experiment. The annealing temperatures were varied between 100 and 160 °C. The increase to 120°C lead to a strong increase in the PCE and J_{SC}, while the PCE stayed in the same range from 120 to 160 °C. However, the J_{SC} increased remarkably at 160 °C. Furthermore, the best cells at 120 and 160 °C showed slight differences in the PCE, the V_{OC} and the FF, but a significant change in the J_{SC} of 0.37 mA. The best cell was annealed for 10 minutes at 160°C, had an active layer thickness of 50 nm, a power conversion efficiency of 3.13%, an open-circuit voltage of 1.04 V and a short-circuit current of 6.96 mA.

The next attempt was trying a donor-to-acceptor ratio of 3:2 and 2:3. The results can be found in Table 23. The best solar cell reached a maximum PCE of 3.42 % with a 3:2 ratio, which is the maximum PCE measured for the two investigated acceptor materials. Generally, the samples with lower acceptor content (3:2 ratio) outperformed those with higher acceptor content (2:3). In comparison, the best solar cell using a 3:2 ratio reached a power conversion efficiency of 3.42%, a open-circuit voltage of 0.99 and a short-circuit current of 7.36 mA with an active layer thickness of 64 nm, while the best solar cell with

Table 22: Influence of rotational speed and annealing temperature on the solar cell characteristics using PMI-DHT-PMI as acceptor material
d:a ratio 1:1, 15 mg/ml, annealing time: 10 minutes
ω...rotational speed, t...thickness, max...maximum values reached

ω / rpm	t / nm	Annealed?	PCE / %	V_{OC} / V	J_{SC} / mA	FF / %
1000	100 ± 19	No	2.28 ± 0.07	1.07 ± 0.02	5.43 ± 0.19	39 ± 1
2400	50 ± 5	No	2.54 ± 0.15	1.11 ± 0.03	5.84 ± 0.12	39 ± 2
		100°C	2.47 ± 0.11	1.07 ± 0.03	5.62 ± 0.14	41 ± 1
		120°C	2.89 ± 0.19	1.09 ± 0.01	6.36 ± 0.36	41 ± 1
		140°C	2.81 ± 0.12	0.97 ± 0.38	6.16 ± 0.27	43 ± 1
		160°C	2.79 ± 0.38	0.97 ± 0.08	7.05 ± 0.10	41 ± 3
		120°C, max	3.10	1.08	6.57	43
		160°C, max	3.13	1.04	6.96	44

a 2:3 ratio achieved only 1.58%, an open-circuit voltage of 1.02 V and only 3.79 mA. The active layer thicknesses were less dependent on the rotational speed than for a 1:1 ratio, although the roughness was significantly higher using a 3:2 or 2:3 ratio compared to the 1:1 ratio. Furthermore, light exposure for 10 minutes did not improve the performance but slightly decreased it.

After one week, the measurements were repeated: The solar cell characteristics changed only slightly (below 10 % difference), thus suggesting good stability in nitrogen atmosphere.

Table 23: Influence of donor-to-acceptor ratios on the solar cell characteristics using PMI-DHT-PMI as acceptor material and applying an annealing step (T=160 °C, t=10 minutes)
d:a ratio 1:1, 15 mg/ml
ω...rotational speed, t...thickness, max...maximum values reached, LS...light-soaking 10 minutes

d:a ratio	ω / rpm	t / nm	Info	PCE / %	V_{OC} / V	J_{SC} / mA	FF / %
3:2	1000	48 ± 2		2.66 ± 0.08	0.80 ± 0.36	6.49 ± 0.30	39 ± 6
	1300	64 ± 18		2.69 ± 0.82	0.88 ± 0.15	7.11 ± 0.30	42 ± 6
			LS	2.19 ± 0.70	0.79 ± 0.16	7.18 ± 0.32	38 ± 6
	1600	51 ± 7		2.86 ± 0.39	0.93 ± 0.03	6.40 ± 0.43	48 ± 3
	1900	51 ± 4		2.74 ± 0.60	0.93 ± 0.06	6.68 ± 0.36	48 ± 7
2:3	1000	54 ± 9		0.83 ± 0.05	1.01 ± 0.02	2.48 ± 0.13	34 ± 1
	1400	63 ± 4		1.08 ± 0.05	0.92 ± 0.02	3.20 ± 0.17	37 ± 1
	1600	38 ± 4		1.46 ± 0.08	0.99 ± 0.03	3.76 ± 0.15	40 ± 1
			LS	1.30 ± 0.15	0.91 ± 0.08	3.63 ± 0.14	39 ± 2
	1900	43 ± 3		1.39 ± 0.08	0.97 ± 0.03	3.43 ± 0.24	42 ± 1
3:2	1300	64 ± 18	max	3.42	0.99	7.36	47
2:3	1600	38 ± 4	max	1.58	1.02	3.79	41

Subsequently, the influence of solvent vapor annealing was analyzed, using a 3:2 donor-to-acceptor ratio (see Table 24). The best solar cell in this case reached a PCE of 2.90%, a V_{OC} of 0.93 V and a J_{SC} of 6.35 mA. Thus, the overall performance was worse than for the cells that were thermally annealed. Furthermore, light-soaking did decrease

the performance of the best cell.

Table 24: Influence of solvent vapor annealing (solvent: CB, T=160 °C, t=10 minutes) on the solar cell characteristics, using PMI-DHT-PMI as acceptor material and a donor-to-acceptor ratio of 3:2.
ω...rotational speed, LS...light-soaking, max...maximum values achieved

ω / rpm	Info	PCE / %	V_{OC} / V	J_{SC} / mA	FF / %
1000		2.51 ± 0.13	1.01 ± 0.02	6.29 ± 0.21	40 ± 1
	LS	2.57 ± 0.17	0.97 ± 0.03	6.73 ± 0.25	40 ± 3
2200		2.75 ± 0.12	0.93 ± 1.11	6.18 ± 0.19	48 ± 2
	LS	2.24 ± 0.13	0.88 ± 0.01	6.21 ± 0.20	0.42 ± 1
1000	max, LS	2.70	0.97	6.94	40
2200	max	2.90	0.93	6.35	49

The external quantum efficiency (EQE) was measured for the best solar cell mentioned in Table 22, using 2400 rpm and thermal annealing (t=10 minutes, T=160°C). In Table 25, one can see the characteristic parameters of the solar cell before and after EQE. The parameters decreased slightly after the EQE measurement, suggesting that the measurement box was not fully sealed and the cell was slightly exposed to oxygen. Since the parameters decreased, it is furthermore assumed, that the solar cell is not stable under ambient air conditions and degrades over time. The EQE measurement suggested a J_{SC} of 6.08 mA/cm^2, which is below the measurement results before and after the EQE measurement but still within the measurement accuracy. The EQE curve shown in Figure 36 depicts the same onsets observed in the UV-vis spectra for the donor-acceptor blend. The maximum is observed at 530 nm with an EQE value of 44.5 %, which is most likely from the acceptor material, while the second maximum is at 628 nm with an EQE value of 33.9 %, which should be caused by the donor material.

Table 25: Characteristic parameters before and after the EQE measurement, 1:1 acceptor-to-donor ratio, PMI-DHT-PMI as acceptor material; 2400 rpm, thermal annealing (t=10 minutes, T=160°C) as shown in Table 22

Measurement	PCE / %	VOC / V	Jsc / mA	FF / %
Before EQE	2.89	1.09	6.36	41
EQE	-	-	6.08	-
After EQE	2.62	1.08	6.20	39

The J-V curve for best solar cell using PMI-DHT-PMI (3:2 ratio, 1300 rpm, 64 nm, as shown in Table 23) can be seen in Figure 37. The red (light) curve exhibits in the first quadrant a quite similar slope as the blue (dark) curve. Furthermore, the red (light) curve is continuously decreasing in the third and fourth quadrant, but not as strong as in case of PMI-3HT-PMI (see Figure 34). According to this plot, the open-circuit voltage is 0.91 V and the short-circuit current is 6.26 mA.

Next, MPP measurements were taken for the duration of 45 minutes, as can be seen in Figure 38. The power conversion efficiency was increasing strongly for the first 25 minutes. Afterwards, the power conversion efficiency started to stabilize. However, a longer

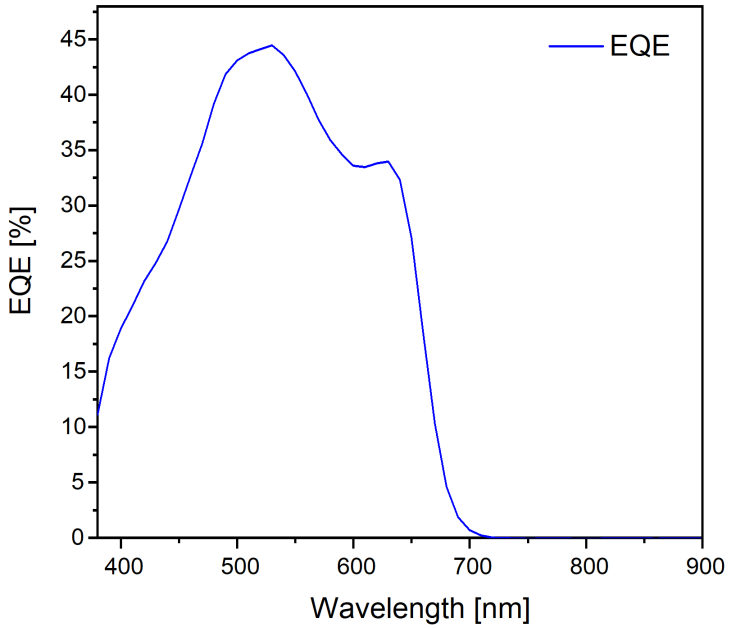

Figure 36: EQE measurement for the best solar cell using PMI-DHT-PMI as the acceptor material

measurement might have shown further increase or decrease of the power conversion efficiency over time. Nonetheless, in comparison to PMI-3HT-PMI, the incident increase of the power conversion efficiency was slower.

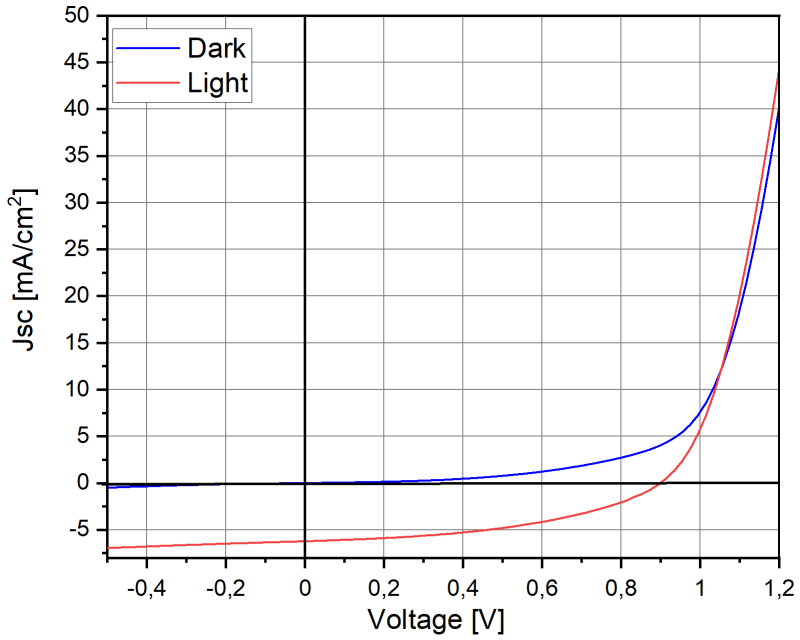

Figure 37: J-V curve for the best solar cell using PMI-DHT-PMI as acceptor material; 3:2 ratio, 1300 rpm, 64 nm, V_{OC}=0.99 V, J_{SC}=7.36 mA, as shown in Table 23

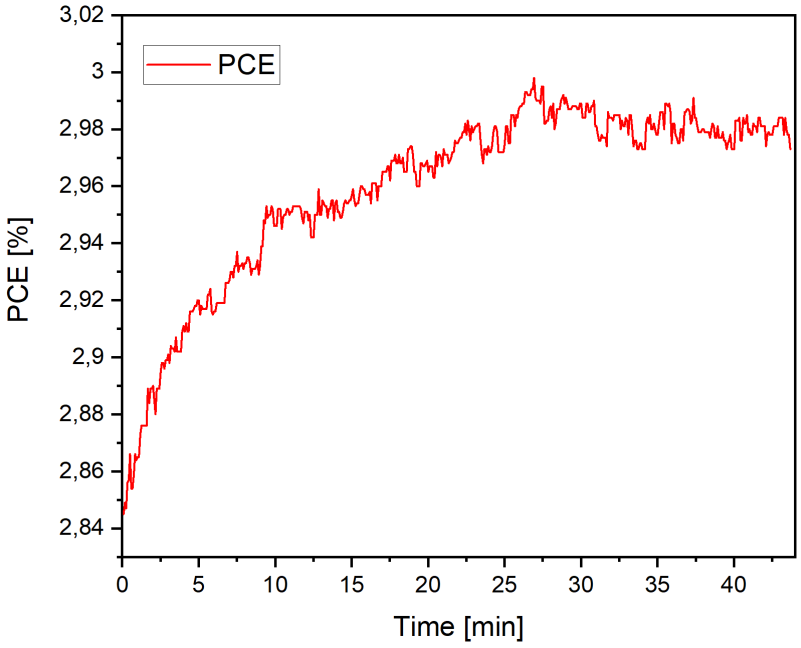

Figure 38: Maximum power point tracking for the solar cells using PMI-DHT-PMI as acceptor material; 3:2 ratio, 1300 rpm, 64 nm, V_{OC}=0.99 V, J_{SC}=7.36 mA, as shown in Table 23

5.4.3 Comparison

The solar cells using PMI-3HT-PMI and PMI-DHT-PMI as acceptor material showed both a better efficiency at about 50 nm in comparison to 78 and 100 nm, respectively, although literature usually suggests 100 nm as the optimum active layer thickness. One possible explanation could be given by the Drift-Diffusion model:
According to this theory, at constant applied voltage, a higher layer thickness is correlated with a lower electric field. [52] Since a lower electric field yields in a lower exciton dissociation rate, thicker active layers can lead to a decrease in the exciton dissociation rate. [52] Furthermore, a higher recombination rate can be observed at higher thicknesses, leading to a lower short-circuit current, which is caused by a higher likelihood of recombination during the longer pathways the charge carriers have to move. [52] Additionally, the lower electric field in thicker layers results in a lower drift diffusion force, meaning that the charge carriers move slower and therefore, the chance of recombination is increasing. [52] In the materials tested in this thesis, the acceptor materials used could be more sensitive to recombination, which could explain the better results at lower than usual active layer thicknesses. Another possibility is, that the materials generally exhibit low conductivity. Furthermore, good phase separation is essential for BHJ organic solar cells but plays a less significant role for thin active layers than for thick active layers: Firstly, the formation of dead ends is more likely for thicker active layers. Secondly, while higher interface area can lead to better efficiencies in organic solar cells, it can also increase the likelihood of recombination. A good phase separation is present in the BHJ if the donor and the acceptor material are well blended but with relatively thick branches. If the branches are too thin, recombination likelihood is increased: In this case, although exciton dissociation is promoted, the free charge carriers are always close to the other phase. In other words the electrons in the acceptor phase will favour to hop back to hole spots, rather than moving further towards the electrode. In thin active layers, this effect is less pronounced: Due to the lower thickness, the path along which recombination can happen is shorter, which leads to decreased recombination probability.

Furthermore, both acceptor materials showed an improvement after thermal annealing and solvent vapor annealing for a 3:2 donor-to-acceptor ratio, although solvent vapor annealing showed greater improvements for the solar cells with thicker active layers, while thermal annealing increased thinner active layers more prominently.
In numbers, for PMI-3HT-PMI solar cells with a thickness of 78 nm and a 1:1 donor-to-acceptor ratio, the substrates without thermal treatments showed a PCE of 0.32 $\pm$ 0.03% and with thermal annealing 0.35 $\pm$ 0.02%. In a 3:2 donor-to-acceptor ratio, the 78 nm substrates with thermal annealing obtained a PCE of 0.34 $\pm$ 0.02% and with solvent vapor annealing 0.65 $\pm$ 0.07%. However, the solar cells with an active layer of only 51 nm achieved a PCE of 0.70 $\pm$ 0.10% without heat treatment, while annealing lead to a decrease to only 0.49 $\pm$ 0.04%. The solar cells built with a 3:2 donor-to-acceptor ratio and

with an active layer thickness of 52 nm exhibited a PCE of 0.69 $\pm$ 0.05% with annealing, while solvent vapor annealing achieved only 0.38 $\pm$ 0.04%.
The acceptor material PMI-DHT-PMI generally performed the best after thermal annealing. Comparing the best cells, the solar cells with a 3:2 ratio and thermal annealing achieved a PCE of 3.42%, while the best solar cell with solvent vapor annealing reached only 2.70%.
Liang et al. investigated the influence of thermal annealing and solvent vapor annealing on the active layer ITIC/PBDB-T and found that solvent vapor annealing mainly enhances the crystallinity of ITIC, while thermal annealing improves the crystallinity of PBDB-T. [51] This suggests, that for the here used acceptor materials, the crystallinity of the donor molecule contributes to a higher extend to the power conversion efficiency. Furthermore, a stronger crystallinity was observed via XRD for PMI-DHT-PMI, explaining the stronger increase of the PCE for PMI-3HT-PMI after solvent vapor annealing compared to PMI-DHT-PMI. Following the results of Liang et al., a two step approach of first applying solvent vapor annealing and then thermal annealing, [51] might have lead to even better morphology and thus better results.

Interestingly, light-soaking for 10 minutes either did not change the PCE for both acceptor materials significantly or lead only to slight de- or increase for both solar cell types, although improvements would have been expected due to charge carrier density enhancement of the ZnO layer. [53] However, it did increase the short-circuit voltage for the 3:2 donor-to-acceptor ratio solar cells for PMI-3HT-PMI as well as PMI-DHT-PMI based solar cells. This increase in the short-circuit current was also observed for ITO/ZnO/P3HT:PCBM/MoO3/Ag based organic solar cells. [54] Symonowicz et al. found, that most likely the amount of dipoles at the interface of ZnO/PCBM increased during light-soaking and lead to an enhanced electric field. [54] This would further result in a better electron collection efficiency and therefore, a higher short-circuit current. [54]
Furthermore, the donor-to-acceptor ratio of 3:2 gave the best results with the high-quality acceptor materials. This could be due to better phase separation with lower acceptor content.

However, the lower-quality acceptor material used in the very first experiment for PMI-3HT-PMI gave a better PCE than the higher-quality acceptor material: In numbers, the greatest achieved PCE 1.10% for the lower-quality PMI-3HT-PMI, while the best cell of the higher-quality PMI-3HT-PMI obtained only a PCE of 0.76%. Taking a look at the layer thicknesses of the the less pure samples, one can see that the active layers are very thin, which could be due to the lower concentration of 10 mg/ml. All in all, the solar cells using PMI-3HT-PMI did not achieve the targeted efficiencies of 2.57%. Since the less pure samples of the first series did achieve better efficiencies, it could be that the acceptor material used by Sanela Alibegic also contained trace impurities. Furthermore, it is known that the

PBDB-T used by Sanela Alibegic was not from the same batch used for this thesis. Another explanation would be that PMI-3HT-PMI is not stable under air or light exposure. In this case, the storage of the sample might have lead to slow degradation.

6 Conclusion and Outlook

The two desired acceptor materials (PMI-3HT-PMI, PMI-DHT-PMI) were successfully synthesized via Suzuki coupling. Both were purified using recrystallization and column chromatography. The yield of PMI-3HT-PMI was 23.5% and it was a dark violett powder. The yield of PMI-DHT-PMI was 26% and it was a dark orange powder. The verification and characterization was done via ^{1}H-NMR spectroscopy, thermogravimetric analysis (TGA), UV-vis spectroscropy and fluorescence spectroscopy:
The TGA measurements depicted a mass loss of 26.7 and 25.1% at 540°C for PMI-3HT-PMI and PMI-DHT-PMI, respectively. Furthermore, PMI-DHT-PMI appeared to be more stable for higher temperatures than PMI-3HT-PMI.
The UV-vis spectra in solution showed for PMI-3HT-PMI a maximum absorption at 530 and 529 nm for PMI-3HT-PMI and PMI-DHT-PMI, respectively. A shoulder was observed at 488 nm for both materials, although it was more pronounced for PMI-DHT-PMI. The UV-vis spectra of the layers were done for the acceptor materials, the donor material and of 1:1 donor-acceptor mixtures: In this case, the absorption spectra of the acceptor materials alone appeared to be similar in shape but the thin film of PMI-DHT-PMI was slightly red shifted towards 533 nm in respect to the solution. The 1:1 mixtures behaved as expected like a sum of the acceptor material and the donor material alone. Thermal treatment revealed a slight red-shift and change in shape and can be seen in Figure 39. This behaviour is due to enhanced crystallinity of the donor material. [51]

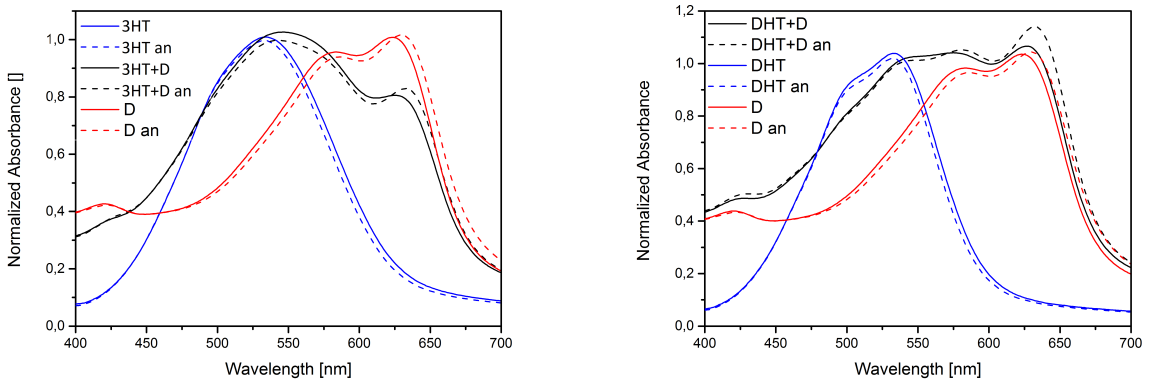

(a) PMI-3HT-PMI

(b) PMI-DHT-PMI

Figure 39: UV-vis absorbance spectra of the annealed (=an) and not annealed layers of both acceptor materials, the donor PBDB-T (=D), and both acceptor-donor mixtures

The fluorescence spectra revealed that the emission maxima were 614 and 590 nm, yielding in a Stokes-shift of 84 and 61 nm for PMI-3HT-PMI and PMI-DHT-PMI, respectively. The quantum yields were found to be 20% and 29%.
The XRD measurements showed, that both acceptor materials do not inhibit pronounced crystallinity. However, thermal annealing lead to slightly enhanced peaks in the spectra.

Besides full characterization, the acceptor materials were used in solar cells together with the donor material PBDB-T in various ratios, different active layer thicknesses and different thermal treatment conditions:
In both cases, the solar cells performed the better at relatively low thicknesses below 65 nm. Furthermore, light-soaking for 10 minutes did not change the performance significantly.
The best cell using PMI-3HT-PMI achieved a PCE of 0.87%, a V_{OC} of 0.65 V and a J_{SC} of 3.37 mA with a thickness of 51 nm, a 1:1 donor-to-acceptor ratio and thermal annealing (10 minutes, 160°C). In case of PMI-3HT-PMI, the donor-acceptor ratio 1:1 performed best, followed by a 3:2 ratio, while the 2:3 ratio performed worst. However, the solar cells using a 3:2 ratio showed only a 0.10% decrease of the PCE. Comparing the behaviour of solvent vapor annealing (solvent: CB, 10 minutes, 160°C) and thermal annealing (10 minutes, 160°C), the solar cells with solvent vapor annealing performed in the same magnitude, although thermally annealed solar cells outperformed solvent vapor annealed solar cells.
The solar cells using PMI-DHT-PMI generally outperformed those using PMI-3HT-PMI: The best solar cell achieved a PCE of 3.42%, a V_{OC} of 0.99 V, a J_{SC} of 7.36 mA with a 3:2 donor-to-acceptor ratio, a thickness of 64 nm and thermal annealing (10 minutes, 160°C). In case of PMI-DHT-PMI, the solar cell performance followed this order: 3:2 $>$ 1:1 $>$ 2:3. Furthermore, thermal annealing strongly improved the performance if the temperature was above 120°C. Additionally, solvent vapor annealing was tested, but did not enhance the solar cell performance as strongly as thermal annealing.
In both cases, light-soaking for 10 minutes did not change the performance significantly.

Taking the synthesis, the purification and the solar cell performance into account, PMI-DHT-PMI outperforms PMI-3HT-PMI in every regard: The synthesis of both materials was straight forward, but in case of PMI-DHT-PMI the formation of by-products was easier to manage. Only a few by-products were formed and purification was straightforward. PMI-3HT-PMI, on the other hand, showed a greater amount of by-products and a by-product that was difficult to extract from the desired product.
Additionally, the performance of PMI-DHT-PMI as acceptor material was significantly better and PMI-DHT-PMI showed greater solubility than PMI-3HT-PMI.

The easy synthesis and performance as well as the promising performance of PMI-DHT-PMI would motivate further investigations. One possibility would be the usage of other donor materials like PCE-10. The donor-to-acceptor ratio could also be varied: Since the best performance was at a 3:2 (=1:0.67) ratio, a 1:0.8 and 1:0.5 would be possible. Furthermore, since solvent vapor annealing was not investigated thoroughly, it could be analyzed at other temperatures as well. Lastly, a combination of thermal annealing and subsequent solvent vapor annealing might improve the performance.

All in all, the PMI-based acceptor materials showed good performance and easy applicability in organic solar cells. Especially PMI-DHT-PMI promises good usability in organic electronics in general.

References

[1] "Ursachen des Klimawandels." [Online]. Available: https://ec.europa.eu/clima/change/causes{_}de

[2] Bundesministerium für Nachhaltigkeit und Tourismus, "Energie in Österreich 2018," *Report*, p. 36, 2018.

[3] L. C. Andreani, A. Bozzola, P. Kowalczewski, M. Liscidini, and L. Redorici, "Silicon solar cells: Toward the efficiency limits," *Advances in Physics: X*, vol. 4, no. 1, 2019. [Online]. Available: https://doi.org/10.1080/23746149.2018.1548305

[4] F. Haase, C. Hollemann, S. Schäfer, A. Merkle, M. Rienäcker, J. Krügener, R. Brendel, and R. Peibst, "Laser contact openings for local poly-Si-metal contacts enabling 26.1%-efficient POLO-IBC solar cells," *Solar Energy Materials and Solar Cells*, vol. 186, pp. 184–193, 2018. [Online]. Available: http://www.sciencedirect.com/science/article/pii/S0927024818303076

[5] K. Yoshikawa, H. Kawasaki, W. Yoshida, T. Irie, K. Konishi, K. Nakano, T. Uto, D. Adachi, M. Kanematsu, H. Uzu, and K. Yamamoto, "Silicon heterojunction solar cell with interdigitated back contacts for a photoconversion efficiency over 26%," *Nature Energy*, vol. 2, no. 5, p. 17032, 2017. [Online]. Available: https://doi.org/10.1038/nenergy.2017.32

[6] R. Hall, "Silicon photovoltaic cells," *Solid-State Electronics*, vol. 24, no. 7, pp. 595–616, jul 1981. [Online]. Available: https://linkinghub.elsevier.com/retrieve/pii/003811018190188X

[7] S. Rafique, S. M. Abdullah, K. Sulaiman, and M. Iwamoto, "Fundamentals of bulk heterojunction organic solar cells: An overview of stability/degradation issues and strategies for improvement," *Renewable and Sustainable Energy Reviews*, vol. 84, pp. 43–53, 2018. [Online]. Available: http://www.sciencedirect.com/science/article/pii/S1364032117315526

[8] L. Meng, Y. Zhang, X. Wan, C. Li, X. Zhang, Y. Wang, X. Ke, Z. Xiao, L. Ding, R. Xia, H.-L. Yip, Y. Cao, and Y. Chen, "Organic and solution-processed tandem solar cells with 17.3% efficiency," *Science*, vol. 361, no. 6407, pp. 1094 LP – 1098, sep 2018. [Online]. Available: http://science.sciencemag.org/content/361/6407/1094.abstract

[9] S. Alibegic, "Synthesis of thiophene and phenyle linked perylenemonoimides as acceptor materials and investigation towards photovoltaic properties," Ph.D. dissertation, 2020.

[10] A. J. Heeger, "25th anniversary article: Bulk heterojunction solar cells: Understanding the mechanism of operation," *Advanced Materials*, vol. 26, no. 1, pp. 10–28, 2014.

[11] K. S. Liao, S. D. Yambem, A. Haldar, N. J. Alley, and S. A. Curran, "Designs and architectures for the next generation of organic solar cells," *Energies*, vol. 3, no. 6, pp. 1212–1250, 2010.

[12] C. Wu, K. Wang, M. Batmunkh, A. S. R. Bati, D. Yang, Y. Jiang, Y. Hou, J. G. Shapter, and S. Priya, "Multifunctional nanostructured materials for next generation photovoltaics," *Nano Energy*, vol. 70, p. 104480, 2020. [Online]. Available: http://www.sciencedirect.com/science/article/pii/S2211285520300379

[13] M. T. Sajjad, A. Ruseckas, and I. D. W. Samuel, "Enhancing Exciton Diffusion Length Provides New Opportunities for Organic Photovoltaics," *Matter*, vol. 3, no. 2, pp. 341–354, 2020. [Online]. Available: http://www.sciencedirect.com/science/article/pii/S259023852030357X

[14] J. Y. Lee, Tack Ho, Park, Song Yi, Park, Won-Woo, Du, Xiaoyan, Son, Jae Hoon, Li, Ning, Kwon, Oh-Hoon, Woo, Han Young, Brabec, Christoph J., Kim, "Efficient Exciton Diffusion in Organic Bilayer Heterojunctions with Nonfullerene Small Molecular Acceptors," *ACS Energy Lett.*, vol. 5, no. 5, pp. 1628–1635, 2020.

[15] M. Sim, J. Shin, C. Shim, M. Kim, S. B. Jo, J.-H. Kim, and K. Cho, "Dependence of Exciton Diffusion Length on Crystalline Order in Conjugated Polymers," *The Journal of Physical Chemistry C*, vol. 118, no. 2, pp. 760–766, jan 2014. [Online]. Available: https://doi.org/10.1021/jp409776s

[16] B. Yang, Y. Yuan, and J. Huang, "Reduced Bimolecular Charge Recombination Loss in Thermally Annealed Bilayer Heterojunction Photovoltaic Devices with Large External Quantum Efficiency and Fill Factor," *The Journal of Physical Chemistry C*, vol. 118, no. 10, pp. 5196–5202, mar 2014. [Online]. Available: https://doi.org/10.1021/jp500547j

[17] S. H. Liao, H. J. Jhuo, P. N. Yeh, Y. S. Cheng, Y. L. Li, Y. H. Lee, S. Sharma, and S. A. Chen, "Single junction inverted polymer solar cell reaching power conversion efficiency 10.31% by employing dual-doped zinc oxide nano-film as cathode interlayer," *Scientific Reports*, vol. 4, pp. 4–10, 2014.

[18] M. Corazza, F. C. Krebs, and S. A. Gevorgyan, "Predicting, categorizing and intercomparing the lifetime of OPVs for different ageing tests," *Solar Energy Materials and Solar Cells*, vol. 130, pp. 99–106, 2014. [Online]. Available: http://www.sciencedirect.com/science/article/pii/S0927024814003407

[19] Y. Şahin, S. Alem, R. de Bettignies, and J.-M. Nunzi, "Development of air stable polymer solar cells using an inverted gold on top anode structure,"

Thin Solid Films, vol. 476, no. 2, pp. 340–343, apr 2005. [Online]. Available: https://linkinghub.elsevier.com/retrieve/pii/S0040609004014452

[20] S. Lattante, "Electron and hole transport layers: Their use in inverted bulk heterojunction polymer solar cells," *Electronics (Switzerland)*, vol. 3, no. 1, pp. 132–164, 2014.

[21] G. Gonçalves, E. Elangovan, P. Barquinha, L. Pereira, R. Martins, and E. Fortunato, "Influence of post-annealing temperature on the properties exhibited by ITO, IZO and GZO thin films," *Thin Solid Films*, vol. 515, no. 24 SPEC. ISS., pp. 8562–8566, 2007.

[22] G. Li, C.-W. Chu, V. Shrotriya, J. Huang, and Y. Yang, "Efficient inverted polymer solar cells," *Applied Physics Letters*, vol. 88, no. 25, p. 253503, jun 2006. [Online]. Available: https://doi.org/10.1063/1.2212270

[23] S. K. Hau, H.-L. Yip, N. S. Baek, J. Zou, K. O'Malley, and A. K.-Y. Jen, "Air-stable inverted flexible polymer solar cells using zinc oxide nanoparticles as an electron selective layer," *Applied Physics Letters*, vol. 92, no. 25, p. 253301, jun 2008. [Online]. Available: https://doi.org/10.1063/1.2945281

[24] A. Mahmood, N. Ahmed, Q. Raza, T. Muhammad Khan, M. Mehmood, M. M. Hassan, and N. Mahmood, "Effect of thermal annealing on the structural and optical properties of ZnO thin films deposited by the reactive e-beam evaporation technique," *Physica Scripta*, vol. 82, no. 6, 2010.

[25] S. Kundu, S. R. Gollu, R. Sharma, G. Srinivas, A. Ashok, A. R. Kulkarni, and D. Gupta, "Device stability of inverted and conventional bulk heterojunction solar cells with MoO3 and ZnO nanoparticles as charge transport layers," *Organic Electronics*, vol. 14, no. 11, pp. 3083–3088, 2013. [Online]. Available: http://dx.doi.org/10.1016/j.orgel.2013.07.016

[26] W. Hou, Y. Xiao, G. Han, and J. Y. Lin, "The applications of polymers in solar cells: A review," *Polymers*, vol. 11, no. 1, pp. 1–46, 2019.

[27] J. Chen, Y. Chen, L.-W. Feng, C. Gu, G. Li, N. Su, G. Wang, S. M. Swick, W. Huang, X. Guo, A. Facchetti, and T. J. Marks, "Hole (donor) and electron (acceptor) transporting organic semiconductors for bulk-heterojunction solar cells," *EnergyChem*, vol. 2, no. 5, p. 100042, 2020. [Online]. Available: http://www.sciencedirect.com/science/article/pii/S2589778020300178

[28] G. Yu, J. Gao, J. C. Hummelen, F. Wudl, and A. J. Heeger, "Polymer Photovoltaic Cells: Enhanced Efficiencies via a Network of Internal Donor-Acceptor Heterojunctions," *Science*, vol. 270, no. 5243, pp. 1789 LP – 1791, dec 1995. [Online]. Available: http://science.sciencemag.org/content/270/5243/1789.abstract

[29] J.-F. Chang, B. Sun, D. W. Breiby, M. M. Nielsen, T. I. Sölling, M. Giles, I. McCulloch, and H. Sirringhaus, "Enhanced Mobility of Poly(3-hexylthiophene) Transistors by Spin-Coating from High-Boiling-Point Solvents," *Chemistry of Materials*, vol. 16, no. 23, pp. 4772–4776, nov 2004. [Online]. Available: https://doi.org/10.1021/cm049617w

[30] S.-H. Liao, Y.-L. Li, T.-H. Jen, Y.-S. Cheng, and S.-A. Chen, "Multiple Functionalities of Polyfluorene Grafted with Metal Ion-Intercalated Crown Ether as an Electron Transport Layer for Bulk-Heterojunction Polymer Solar Cells: Optical Interference, Hole Blocking, Interfacial Dipole, and Electron Conduction," *Journal of the American Chemical Society*, vol. 134, no. 35, pp. 14 271–14 274, sep 2012. [Online]. Available: https://doi.org/10.1021/ja303813s

[31] Z. Zheng, H. Yao, L. Ye, Y. Xu, S. Zhang, and J. Hou, "PBDB-T and its derivatives: A family of polymer donors enables over 17% efficiency in organic photovoltaics," *Materials Today*, vol. 35, no. May, 2019.

[32] Suman, A. Bagui, A. Garg, B. Tyagi, V. Gupta, and S. P. Singh, "A fluorene-core-based electron acceptor for fullerene-free BHJ organic solar cells - Towards power conversion efficiencies over 10%," *Chemical Communications*, vol. 54, no. 32, pp. 4001–4004, 2018.

[33] S. Gélinas, T. S. V. D. Poll, G. C. Bazan, and R. H. Friend, "Ultrafast Long-Range Charge Photovoltaic Diodes," vol. 512, no. January, pp. 512–517, 2014.

[34] J. Hou, O. Inganas, R. H. Friend, and F. Gao, "Organic solar cells based on non-fullerene acceptors," *Nature Materials*, vol. 17, no. 2, pp. 119–128, 2018.

[35] C. Kirmaier, H. E. Song, E. Yang, J. K. Schwartz, E. Hindin, J. R. Diers, R. S. Loewe, K. Y. Tomizaki, F. Chevalier, L. Ramos, R. R. Birge, J. S. Lindsey, D. F. Bocian, and D. Holten, "Excited-state photodynamics of perylene-porphyrin dyads. 5. tuning light-harvesting characteristics via perylene substituents, connection Motif, and three-dimensional architecture," *Journal of Physical Chemistry B*, vol. 114, no. 45, pp. 14 249–14 264, 2010.

[36] J. Cremer, E. Mena-Osteritz, N. G. Pschierer, K. Müllen, and P. Bäuerle, "Dye-functionalized head-to-tail coupled oligo(3-hexylthiophenes) - Perylene-oligothiophene dyads for photovoltaic applications," *Organic and Biomolecular Chemistry*, vol. 3, no. 6, pp. 985–995, 2005.

[37] Y. Hu, S. Chen, L. Zhang, Y. Zhang, Z. Yuan, X. Zhao, and Y. Chen, "Facile Approach to Perylenemonoimide with Short Side Chains for Nonfullerene Solar Cells," *Journal of Organic Chemistry*, vol. 82, no. 11, pp. 5926–5931, 2017.

[38] R. Qin, D. Guo, M. Li, G. Li, Z. Bo, and J. Wu, "Perylene monoimide dimers enhance ternary organic solar cells efficiency by induced D-A crystallinity," *ACS Applied Energy Materials*, vol. 2, no. 1, pp. 305–311, 2019.

[39] X. Guo, A. Facchetti, and T. J. Marks, "Imide- and amide-functionalized polymer semiconductors," *Chemical Reviews*, vol. 114, no. 18, pp. 8943–9012, 2014.

[40] B. Schweda, "Phenylene-Linked Perylene-Monoimide based Acceptors for the Application in Organic Solar Cells," Ph.D. dissertation, Technical University of Graz, 2019.

[41] P. Fürk, "Enhancing the Permittivity of Perylene-Linker-Perylene Acceptors for Application in Organic Solar Cells," Ph.D. dissertation, 2020.

[42] S. Weber, J. Hofinger, T. Rath, M. Reinfelds, D. Pfeifer, S. Borisov, P. Fürk, H. Amenitsch, M. Scharber, and G. Trimmel, "Comparison of Fluorene, Silafluorene and Carbazol as Linkers in Perylene Monoimide Based Non-Fullerene Acceptors," *Advanced Materials*, 2020.

[43] Y. Zhang, X. Guo, B. Guo, W. Su, M. Zhang, and Y. Li, "Nonfullerene Polymer Solar Cells based on a Perylene Monoimide Acceptor with a High Open-Circuit Voltage of 1.3 V," *Advanced Functional Materials*, vol. 27, no. 10, p. 1603892, mar 2017. [Online]. Available: https://doi.org/10.1002/adfm.201603892

[44] Q. Liu, Y. Jiang, K. Jin, J. Qin, J. Xu, W. Li, J. Xiong, J. Liu, Z. Xiao, K. Sun, S. Yang, X. Zhang, and L. Ding, "18% Efficiency organic solar cells," *Science Bulletin*, vol. 65, no. 4, pp. 272–275, 2020. [Online]. Available: http://www.sciencedirect.com/science/article/pii/S2095927320300013

[45] J. Frisch, M. J. , Trucks, G. W., Schlegel, H. B. , Scuseria, G. E., Robb, M. A., Cheeseman, J. R., Scalmani, G., Barone, V., Mennucci, B., Petersson, G. A., Nakatsuji, H., Caricato, M., Li, X., Hratchian, H. P., Izmaylov, A. F. , Bloino, J., Zheng, G. , Son and D. J. Fox, "Gaussian 09," 2013.

[46] M. Moreno-Mañas, M. Pérez, and R. Pleixats, "Palladium-catalyzed suzuki-type self-coupling of arylboronic acids. A mechanistic study," *Journal of Organic Chemistry*, vol. 61, no. 7, pp. 2346–2351, 1996.

[47] X. Yang, X. Dou, and K. Müllen, "Efficient synthesis of symmetrically and unsymmetrically substituted hexaphenylbenzene analogues by Suzuki-Miyaura coupling reactions," *Chemistry - An Asian Journal*, vol. 3, no. 4, pp. 759–766, 2008.

[48] H. J. Reich and D. J. Cram, "Macro Rings. XXXVI. Ring Expansion, Racemization, and Isomer Interconversions in the [2.2]Paracyclophane System through a Diradical Intermediate," *Journal of the American Chemical Society*, vol. 91, no. 13, pp. 3517–3526, 1969.

[49] F. Banishoeib, A. Henckens, S. Fourier, G. Vanhooyland, M. Breselge, J. Manca, T. J. Cleij, L. Lutsen, D. Vanderzande, L. H. Nguyen, H. Neugebauer, and N. S. Sariciftci, "Synthesis of poly(2,5-Thienylene Vinylene) and its derivatives: Low band gap materials for photovoltaics," *Thin Solid Films*, vol. 516, no. 12, pp. 3978–3988, 2008.

[50] D. Blakemore, *Suzuki – Miyaura Coupling*, 2016, vol. 1, no. 52.

[51] Q. Liang, J. Han, C. Song, X. Yu, D.-M. Smilgies, K. Zhao, J. Liu, and Y. Han, "Reducing the confinement of PBDB-T to ITIC to improve the crystallinity of PBDB-T/ITIC blends," *Journal of Materials Chemistry A*, vol. 6, no. 32, pp. 15 610–15 620, 2018. [Online]. Available: http://dx.doi.org/10.1039/C8TA05892J

[52] Y. Min Nam, J. Huh, and W. Ho Jo, "Optimization of thickness and morphology of active layer for high performance of bulk-heterojunction organic solar cells," *Solar Energy Materials and Solar Cells*, vol. 94, no. 6, pp. 1118–1124, 2010. [Online]. Available: http://www.sciencedirect.com/science/article/pii/S0927024810000942

[53] Z. Jiang, S. Soltanian, B. Gholamkhass, A. Aljaafari, and P. Servati, "Light-soaking free organic photovoltaic devices with sol–gel deposited ZnO and AZO electron transport layers," *RSC Advances*, vol. 8, no. 64, pp. 36 542–36 548, 2018. [Online]. Available: http://dx.doi.org/10.1039/C8RA07071G

[54] J. Symonowicz, M. Morawski, M. Dusza, P. Peksa, A. Sieradzki, and F. Granek, "Investigation of the light-soaking effect in organic solar cells using dielectric permittivity and electric modulus approaches," *Organic Electronics*, vol. 52, pp. 32–41, 2018. [Online]. Available: http://www.sciencedirect.com/science/article/pii/S156611991730486X

Appendix

List of Figures

List of Tables

Analytical Data

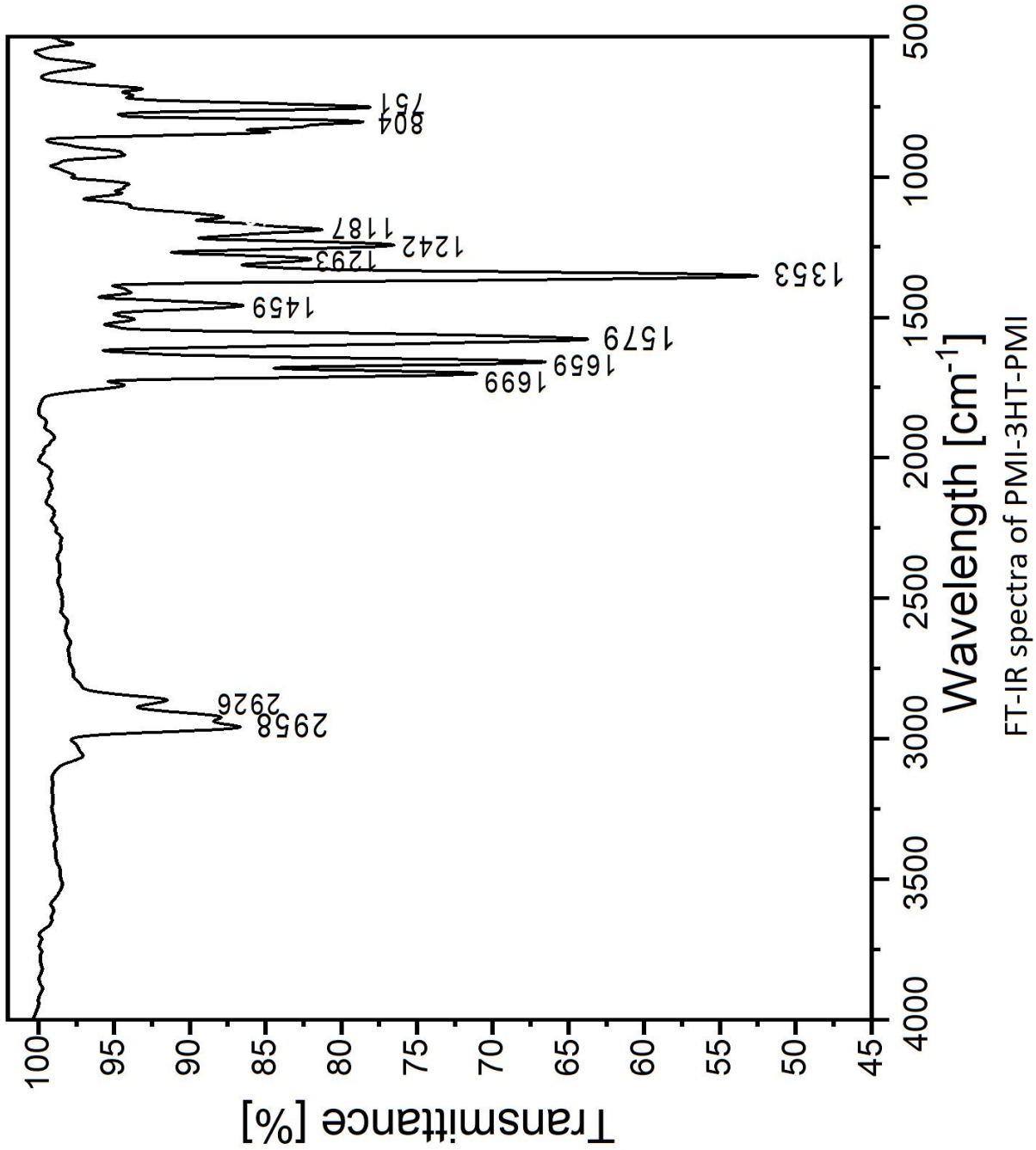

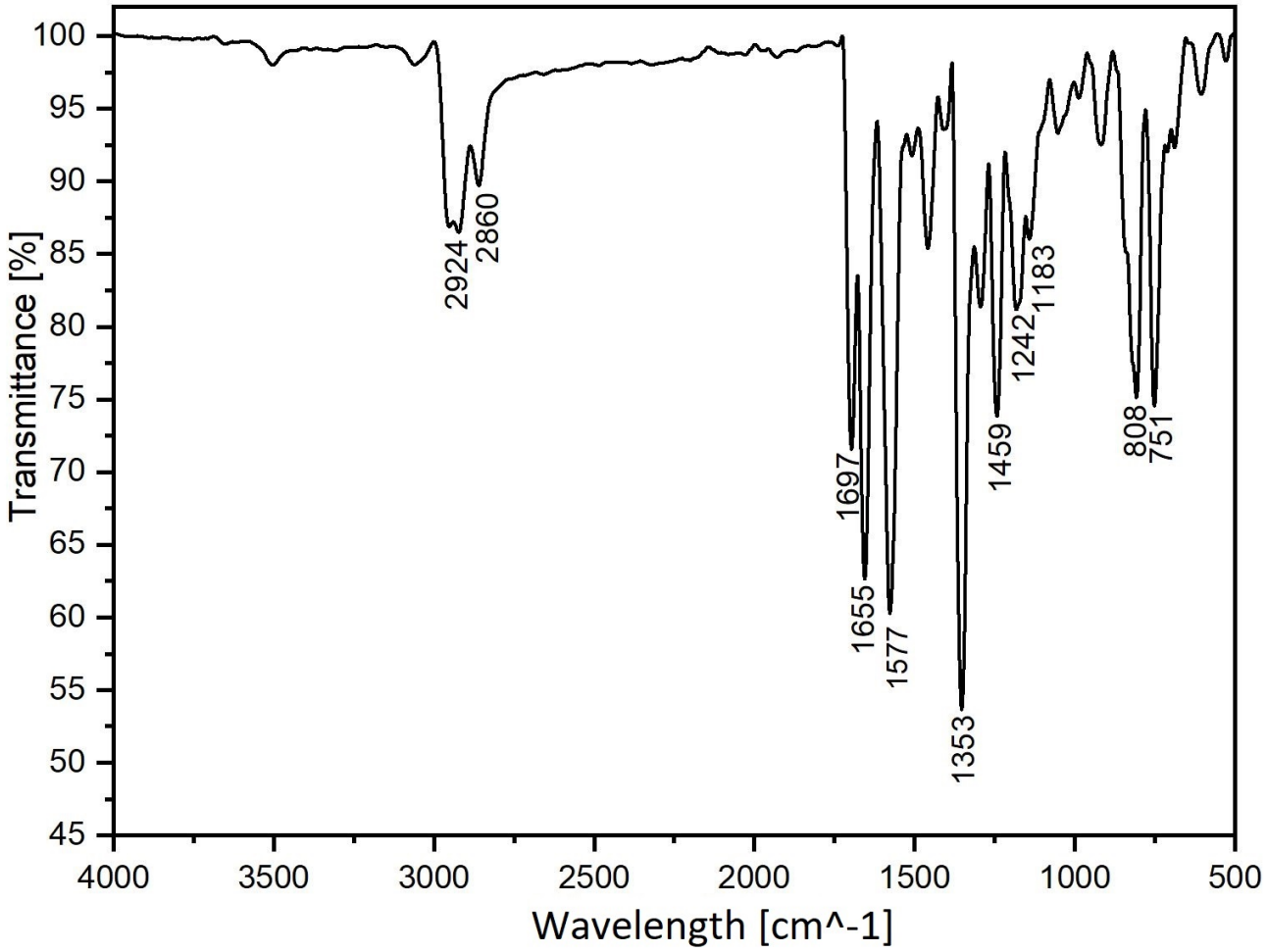

FT-IR spectra of PMI-DHT-PMI

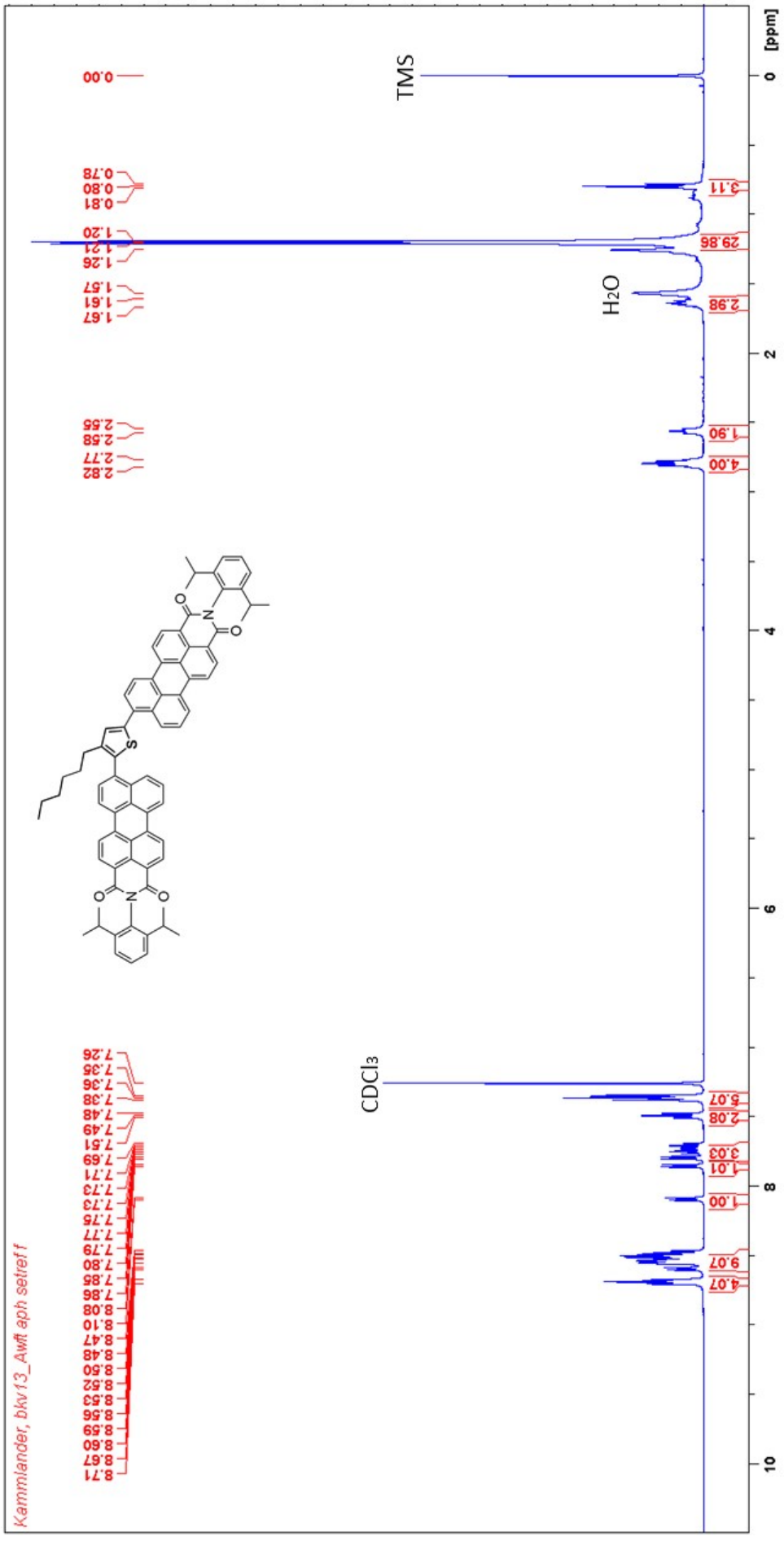
TMS
H2O
CDCl3
[ppm]
Kammlander, bkv13_Awft aph seltref f

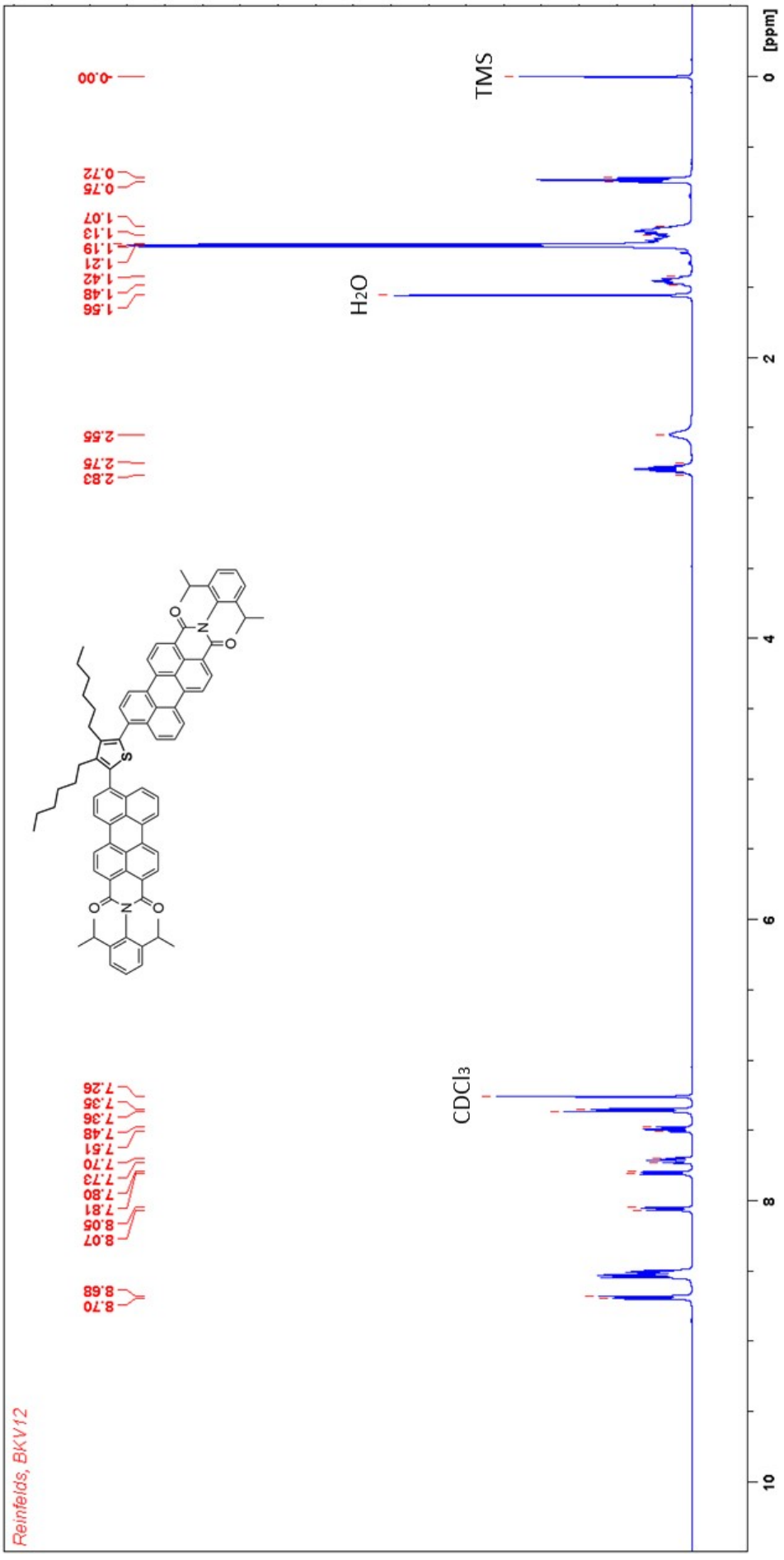
Reinfelds, BKV12
8.70
8.68
8.07
8.05
7.81
7.80
7.73
7.70
7.51
7.48
7.36
7.35
7.26
2.83
2.75
2.55
1.56
1.48
1.42
1.21
1.19
1.13
1.07
0.75
0.72
0.00
CDCl3
H2O
TMS
[ppm]
0
2
4
6
8
10